UNIVERSITA' DEGLI STUDI DI PADOVA

DIPARTIMENTO DI FISICA E ASTRONOMIA "GALILEO GALILEI"

Corso di Laurea in Fisica

Tesi di Laurea

First characterization of the SPIDER negative ion beam by the diagnostic calorimeter STRIKE

Relatore:
Dr. Gianluigi Serianni

Correlatore:
Dr. Antonio Pimazzoni

Laureando:
Gloria Canocchi

Anno Accademico 2018/2019

Abstract

The ITER tokamak is an international project, whose aim is to prove the possibility to produce energy by nuclear fusion of deuterium and tritium nuclei with a sufficient efficiency and for a reasonable duration of time (up to one hour for ITER). In order to reach the high temperatures necessary for thermonuclear fusion, additional heating systems are required, such as the injection of a neutral beam. The main component of a Neutral Beam Injector (NBI) is a Radio Frequency (RF) source which creates negative hydrogen or deuterium ions. The test facility SPIDER (*Source for the Production of Ions of Deuterium Extracted from a Radio frequency plasma*) was built at Consorzio RFX in Padova (Italy), in order to study and optimize negative ion production and extraction for the ITER neutral beam injectors. In order to measure the parameters of the SPIDER negative ion beam, several diagnostics are used. One of them is the *Short-Time Retractable Instrumented Kalorimeter Experiment* (STRIKE) with the aim of characterizing the SPIDER beam during short operations (several seconds) and verifying the ITER requirement regarding the maximum allowed beam non-uniformity (below $\pm 10\%$). The most important measurements performed by STRIKE are: beam uniformity and current, beam divergence and particle losses due to the beam interaction with the background gas. The main components of STRIKE are 16 one-directional (1D) Carbon Fiber Composite (CFC) tiles, observed on the rear side by thermal cameras in order to determine the spatial distribution of power within the beam, constituted by 4×4 groups of 5 (horizontally) $\times$ 16 (vertically) beamlets each.
The main goal of the present thesis is to give a first characterization of the SPIDER negative ion beam by means of the STRIKE calorimeter.
In *Chapter 1*, an introduction to nuclear fusion and to the ITER experiment is given. Furthermore the magnetic confinement is explained, focusing on the Neutral Beam Injector (NBI) heating of the fusion plasma.
Negative ion sources and beam physics are described in *Chapter 2*, in particular the creation of negative hydrogen ions H^- is explained.
Chapter 3 presents the technical details of the negative ion source SPIDER and the STRIKE calorimeter, focusing on the tiles and the diagnostics provided by STRIKE.
In *Chapter 4* the software used for the data analysis of the first phase of experimental activity is described.
Data analysis is then discussed in *Chapter 5*: in particular the influence of the source parameters on the beam properties is investigated.
Finally, the main results and the future developments are presented in *Chapter 6*.

Sommario

Il tokamak ITER (*International Thermonuclear Experimental Reactor*) è un progetto internazionale, il cui obiettivo è quello di dimostrare la possibilità di produrre energia mediante la fusione nucleare di nuclei di deuterio e trizio con un'efficienza sufficiente e per un tempo ragionevole (fino a un'ora per ITER). Per raggiungere le temperature necessarie alla fusione, occorrono dei sistemi di riscaldamento addizionali, quale ad esempio l'iniezione di un fascio di particelle neutre. Il cuore di un iniettore di neutri (NBI) è una sorgente a radiofrequenza che crea ioni negativi di idrogeno e/o deuterio. Il prototipo di tale sorgente, SPIDER (*Source for the Production of Ions of Deuterium Extracted from a Radio frequency plasma*), è stato costruito al Consorzio RFX di Padova per studiare e ottimizzare la produzione di ioni negativi e la loro estrazione dalla sorgente. Per misurare i parametri del fascio di ioni negativi di SPIDER, sono utilizzati diversi strumenti diagnostici. Uno di essi è il calorimetro STRIKE (*Short-Time Retractable Instrumented Kalorimeter Experiment*) il cui obiettivo è caratterizzare il fascio di SPIDER durante brevi operazioni (di qualche secondo) e verificare che il fascio rispetti i requisiti di ITER per quanto riguarda la massima non uniformità consentita (meno del $\pm 10\%$). Le misure più importanti svolte da STRIKE riguardano: l'uniformità e la corrente del fascio, la sua divergenza e le perdite dovute all'interazione tra il fascio e il gas di fondo. Le principali componenti di STRIKE sono 16 tegole in fibra di carbonio composita (1D-CFC), osservate sul retro da delle termocamere al fine di determinare la distribuzione spaziale della potenza all'interno del fascio, costituito da 1280 fascetti, divisi in 4×4 gruppi di 5×16 *beamlets* ciascuno.
L'obiettivo principale di questa tesi è dare una prima caratterizzazione del fascio di ioni negativi di SPIDER mediante il calorimetro STRIKE.
Nel *Capitolo 1*, viene data un'introduzione alla fusione nucleare e all'esperimento ITER. Viene inoltre data la definizione di plasma e viene spiegato il confinamento magnetico, focalizzandosi sui requisiti e sui componenti di un iniettore di un fascio di neutri (NBI).
Le sorgenti di ioni negativi e la fisica di un fascio di particelle vengono descritte nel *Capitolo 2*, dove è posta particolare attenzione alla creazione di ioni idrogeno negativi H^-.
Il *Capitolo 3* presenta i dettagli tecnici della sorgente di ioni negativi SPIDER e del calorimetro STRIKE, focalizzandosi sulle tegole e sulle diagnostiche eseguite da tale calorimetro.
Nel *Capitolo 4* viene descritto il software utilizzato per l'analisi dei dati di STRIKE durante la prima fase di attività sperimentale.
L'analisi dati viene poi discussa nel *Capitolo 5*: in particolare si studia l'influenza dei parametri della sorgente sulle proprietà del fascio.
Infine i principali risultati e gli studi futuri sono presentati nel *Capitolo 6*.

Contents

1 Introduction

In this section, an introduction to nuclear fusion and to the ITER experiment is given, focusing on the Neutral Beam Injector (NBI) heating of the fusion plasma.

1.1 Nuclear fusion

The energy problem is one of the most critical topic of the last years: actually about the 85% of the primary energy comes from fossil fuels. Considering the increase of the energy demand and the issues related to environmental pollution, any alternative energy source should be studied carefully. The nuclear fusion, or thermonuclear reaction, is one of the possibilities.
Nuclear fusion is the process in which two light nuclei (protons, deuterium, helium) merge, releasing energy. In particular, the primary source of solar energy, is the fusion of hydrogen to form helium (the proton-proton chain reaction), which produces considerable energy release which sustains life on Earth. The main aim of the research on nuclear fusion is to reproduce, in a controlled way, processes similar to those occurring in stars, in order to obtain a safe and environmentally friendly energy source. In experimental laboratories, for fusion reactions, two hydrogen isotopes are used: deuterium D and tritium T nuclei. They indeed show the highest cross section in fusion reactions (see Fig. 1(a)) and they have an activation energy lower than other reactions.

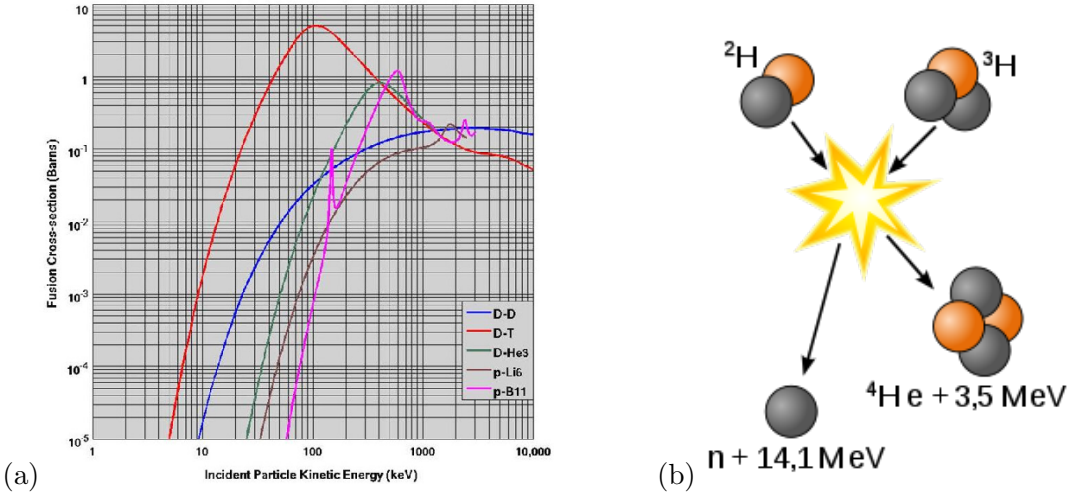

Figure 1: (a) Cross sections of various fusion reactions as a function of the kinetic energy of an incident particle on a stationary target [1] ;(b) Illustration of the fusion reaction between deuterium and tritium nuclei [2].

As shown in Fig. 1(b), the fusion reaction between deuterium and tritium nuclei is:

$$^2\mathrm{D} +^3 \mathrm{T} \rightarrow \mathrm{He}(3.5\ \mathrm{MeV}) + \mathrm{n}(14.1\ \mathrm{MeV}) \tag{1}$$

While deuterium is available in the seawater (a certain percentage of H_2O molecules in nature are indeed D_2O), tritium is not available in large quantities: it is not a stable isotope (in fact it has an half-life time of 12.3 years). Hence, it is necessary to create these nuclei using lithium Li, an element which is widely available in the Earth's crust and in the oceans:

$$\mathrm{n} +^6 \mathrm{Li} \rightarrow^4 \mathrm{He}(2.05\ \mathrm{MeV}) +^3 \mathrm{T}(2.75\ \mathrm{MeV}) \tag{2}$$

1.2 Definition of Plasma

In a fusion reactor, there are very high temperatures, at which matter is in the state of *plasma*: a quasi-neutral gas of charged particles (positive nuclei and negative electrons), partly or fully ionized, displaying a collective behaviour. The quasi-neutrality condition implies the absence of macroscopic

concentration of charge, which means that the density of positive and negative particles is the same ($n_{ions} \approx n_{electrons}$). Furthermore, if a charged object is inserted into a plasma, it is surrounded by charges of the opposite sign, so that it is shielded from the rest of the ionized gas: for example, if the object is negatively charged, in its neighbourhood electrons will be repelled while ions will be attracted.
The characteristic length for the screening of charged objects immersed in ionized gas is called *Debye length*:

$$\lambda_D = \sqrt{\frac{\epsilon_0 k_B T_e}{n e^2}} \tag{3}$$

where ϵ_0 is the permittivity of free space, k_B is the Boltzmann constant, T_e and e are the electron temperature and charge respectively, n is the plasma density, the same for negatively and positively charged particles.
The Debye length is also the typical length over which charge imbalance may exist in ionized gas. Neutrality is violated inside the *Debye sphere* (of radius λ_D), but outside quasi-neutrality prevails if the number of charged particles N_D in the Debye sphere satisfies the condition:

$$N_D = \frac{4}{3}\pi \lambda_D^3 n >> 1 \tag{4}$$

In fact this implies that it is possible to calculate meaningful averages of physical quantities.
Another main parameter is the *plasma frequency* $\omega_{p,e}$: it is the natural oscillation frequency of electrons in a plasma, in response to small charge separations:

$$\omega_{p,e} = \sqrt{\frac{n_e e^2}{\epsilon_0 m_e}} \tag{5}$$

where m_e and n_e are the electron mass and density, respectively. Dimensionally, the real frequency is: $\nu_{p,e} = \frac{\omega_{p,e}}{2\pi}$.
An oscillation frequency for ions is defined analogously: $\omega_{p,i}$. But, since the oscillation frequency is proportional to the inverse square root of the particle mass, it appears that $\omega_{p,i} << \omega_{p,e}$.
If an electromagnetic radiation with frequency ν enters a slab of ionized gas having density n, electrons can absorb the wave energy and then re-emit it if $\nu < \frac{\omega_{p,e}}{2\pi}$. On the contrary case, electrons can not follow the wave oscillation so the wave propagates through slab undisturbed. If instead, the wave frequency is exactly the same of the plasma frequency, electrons absorb all the energy and then they heat the plasma through collisions with other particles. This means that it is possible to couple a certain power to a plasma by means of electromagnetic waves of proper frequency.
If ν_c is the particles *collision frequency*, a plasma must satisfy another condition:

$$\frac{\omega_p}{\nu_c} > 1 \tag{6}$$

This implies that collisions are less frequent than plasma oscillations, so that it is possible to study the ionized gas with electromagnetism and hydrodynamics together.

1.2.1 Magnetic Confinement

There are two different methods to reach meaningful density and temperature in order to have a reasonable number of fusion reactions:

- Inertial Confinement Fusion (*ICF*): it is based on the compression and heating of a nuclear fuel, often made of deuterium and tritium, hit by many laser beams at high intensity.
- Magnetic Confinement: it is based on the use of magnetic fields to confine a plasma in the shape of a torus, in order to reduce the losses of charged particles and keeping them away from the inner walls of the device. The scheme of a toroidal geometry is shown in Fig. 2.

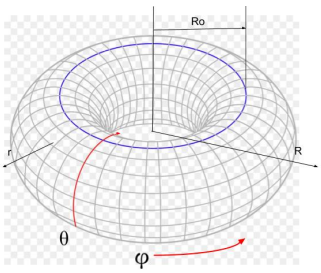

Figure 2: Scheme of a toroidal geometry

In a plasma in fact, charged particles feel the magnetic field and revolve around the magnetic field lines following orbits with a radius r_L, called *Larmor radius* (Eq. (14)).
In general, two different experimental designs for magnetic confinement exist: tokamak and stellarator. In both the devices, two magnetic fields are used:

- A toroidal field, produced by coils that surround the torus B_ϕ
- A poloidal field, in the plane orthogonal to the toroidal field B_θ (see Fig. 2).
  The reference design for the first experimental nuclear fusion reactor ITER (more details later) is a tokamak. In this device, the poloidal field is created by the electric toroidal current which flows inside the plasma. This current is induced by varying the current in the solenoid at the center of torus. The two devices, tokamak and stellarator, are represented in Fig. 3:

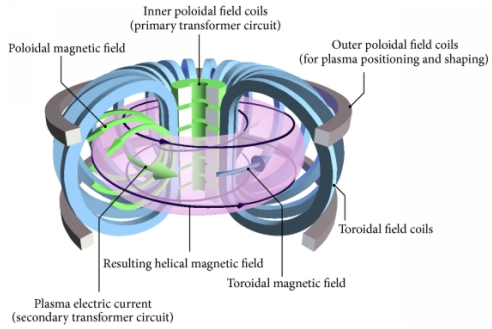

(a)

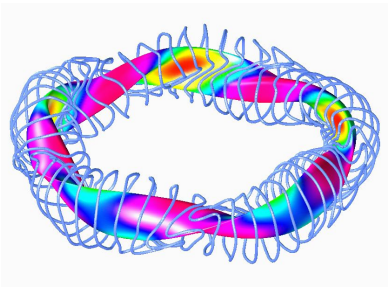

(b)

Figure 3: Illustration of the two devices based on magnetic confinement: tokamak (a) [5] and stellarator Wendelstein 7-X (Germany) (b) [6]. for this one, the colors correspond to the magnetic field intensity: blue means high while red means low intensity.

The first experimental nuclear fusion reactor is the tokamak ITER, represented in Fig. 4. It is an international project under construction in Cadarache (France). Operation on ITER will be based on deuterium and tritium reactions, in order to create a plasma with a *Q value*[1] (fusion energy gain factor) larger than 10.
The plasma will be confined inside a vacuum vessel by the magnetic field. The vessel is surrounded by coils, that create the toroidal and poloidal fields, immersed in a cryostat (with liquid helium in a supercritical state, around 4K [16]), where they are shielded from the neutrons produced in the fusion reaction.

[1]The Q value is the ratio between the fusion power produced by the reactor and the auxiliary power required to sustain the reaction itself.

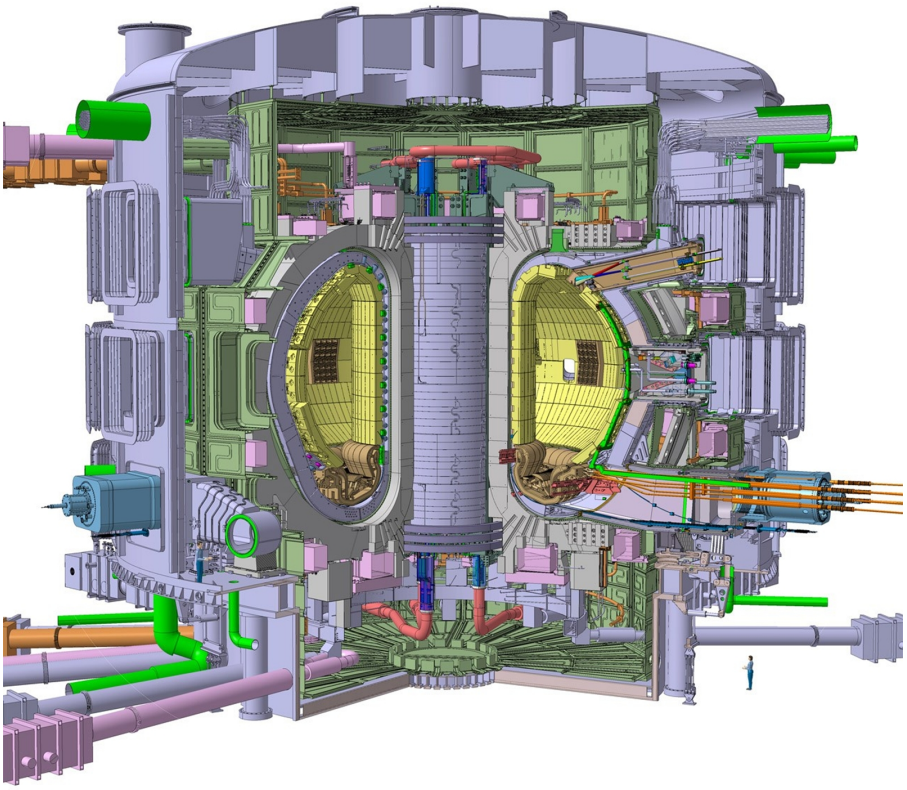

Figure 4: Design of ITER fusion reactor [16]

For a reactor, external injected power is needed. Moreover, the energy confinement time is linked with the tokamak size, so ITER, thanks to its large dimensions (summarized in Tab. 1), will be the first device able to achieve a confinement time in the range of 4-6 s.

ITER parameters	Value
Fusion Power	500 MW
Fusion power gain (Q)	≥ 10
Pulse duration	3600 s
Type of plasma	D-T
Plasma major radius	6.2 m
Plasma minor radius	2.0 m
Plasma current	15 MA
Toroidal field at R = 6.2 m	5.3 T
Installed auxiliary heating:	
- by neutral beam injection	33 MW
- by radio-frequency waves	40 MW
Plasma Volume	830 m^3
Plasma surface area	680 m^2
Machine height	26 m
Machine diameter	29 m

Table 1: ITER parameters and operational capabilities [16]

ITER neutral beam requirements and parameters	Value
Source dimensions	1.9×0.9 m^2
Source pressure	0.3 Pa
Extraction area	0.2 m^2
Extracted current	58 A for D$^-$ beam
	68 A for H$^-$ beam
Accelerated current	40 A for D$^-$ beam
	49 A for H$^-$ beam
Fraction of co-extracted electrons (j_e/j_{ion})	≤ 1
Pulse duration	3600 s
Uniformity	$\pm 10\%$
Divergence	≤ 7 mrad

Table 2: ITER neutral beam requirements [16]

1.3 Neutral Beam Injectors (NBI)

Although the plasma current in toroidal direction heats the plasma by ohmic heating, the temperature which can be reached, is not sufficient to have a satisfactory rate of fusion reactions. For this reason, external heating systems are required.
The plasma heating can be done in different ways (see Fig. 5): for example, using high-frequency electromagnetic waves (RF) or using neutral beam injectors (NBI).

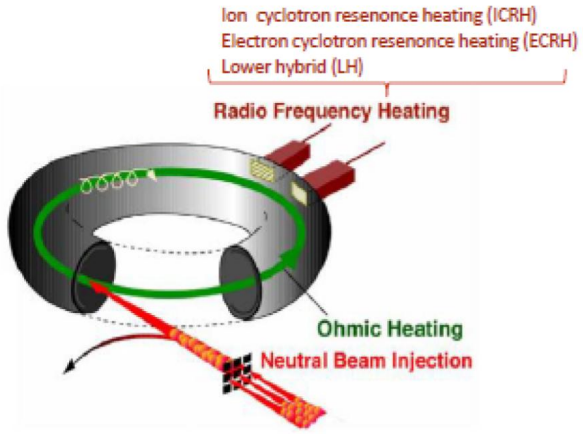

Figure 5: Illustration of the main plasma heating systems in a tokamak: the ohmic heating, the Radio Frequency (RF) heating and the neutral beam injection heating [3].

The last heating method consists in injecting high-energy atoms (hydrogen or deuterium) into the magnetically confined plasma.
In order to avoid deflections by the magnetic field, the injected particles must be *neutral*, so that they can reach the plasma and be ionized through collisions with electrons and ions.
NBI heating is dominant in most large past, present, and planned tokamaks as shown in Tab. 3:

	Major radius [m]	Minor radius [m]	I_{plasma} [MA]	B [T]	Positive-NBI [MW]	Negative-NBI [MW]	RF wave heating [MW]
ITER	6.2	2.0	15	5.3	-	33	20
JET	2.96	1.25	4.8	3.45	34	-	10
JT-60U	3.4	1.1	5	4.2	40	3	7
JT-60SA	2.97	1.17	5	2.25	24	10	7
TFTR	2.4	0.8	2.2	5	40	-	11
EAST	1.7	0.4	1.0	3.5	-	-	3
ASDEX Upgrade	1.65	0.65	1.2	3.1	20	-	7

Table 3: Main parameters of the most important Tokamaks: data from W. Kraus, CERN Accelerator School - Ion Sources (2012) [3]

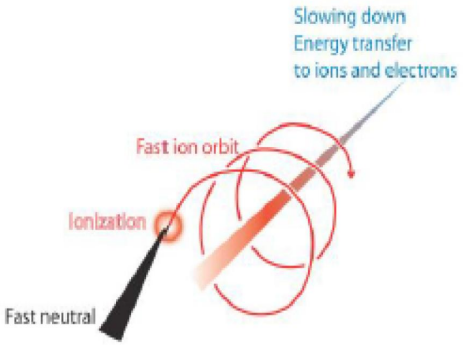

Figure 6: Representation of the interaction of fast neutrals with the plasma [3]

Considering a hydrogen beam, the possible interactions with the plasma ions are the following:

- the charge exchange reaction: $\mathrm{H_{beam} + H^+_{plasma} \rightarrow H^+_{beam} + H_{plasma}}$
- the ionization by plasma ions: $\mathrm{H_{beam} + H^+_{plasma} \rightarrow H^+_{beam} + H^+_{plasma} + e^-}$
- the ionization by plasma electrons: $\mathrm{H_{beam} + e^- \rightarrow H^+_{beam} + 2e^-}$

The *absorption law* describes the decay of the neutral beam intensity $I_{beam}(x)$ inside the plasma:

$$\frac{dI_{beam}}{dx} = -n\sigma_s I_{beam} \tag{7}$$

The solution is: $I_{beam}(x) = I_0 e^{-\frac{x}{\lambda}}$
where I_0 is the initial beam intensity, $\lambda = \frac{1}{n\sigma_s}$ is the e-folding length of the beam attenuation, n is the ion density. Moreover:

$$\sigma_s = \sigma_{ex} + \sigma_i + \frac{\langle \sigma_e v_e \rangle}{v_{beam}} \tag{8}$$

where σ_{ex}, σ_i, $\langle \sigma_e v_e \rangle$ and v_{beam} are the charge exchange cross section, the ionization cross section by ions, the electron ionization rate coefficient and the beam speed, respectively.
The main components of a Neutral Beam Injector (NBI) are represented in Fig. 7:

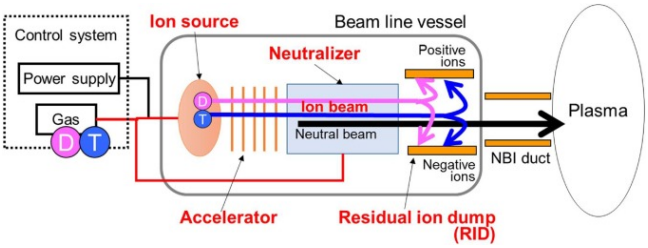

Figure 7: Illustration of the main components of a Neutral Beam Injector of deuterium and tritium nuclei[4].

Proceeding from left to right in Fig. 7, there is: the beam source where negative ions are created, then they are accelerated to the desired energy through a system made of grids at different potential. After that, a fraction of the ions is neutralized through collisions with the background gas, in the neutralizer. Right after it, there is a magnetic field (or electrostatic field in the case of ITER) that deflects the residual ions, which are collected by the Residual Ion Dump (RID), before the beam reaches the plasma in the tokamak.
The efficiency of the neutralization process is different for positive and negative ion beams, as shown in Fig. 8. At low energies, the neutralization efficiency is the same for both the type of ions, however at energies higher than 100 keV, for positive ions, it decreases rapidly to almost zero for energies around 1 MeV. On the other hand, negative ion beams maintain a neutralization efficiency of about 60 % even at high energies. This is due to the low binding energy of electrons, equal to 0.75 eV. For this reason, a negative ion source was chosen for the ITER NBI system.
Moreover it may be noticed from Table 3 as positive ion NBIs are used in the devices with smaller major radius, in which the required penetration depth is usually smaller.

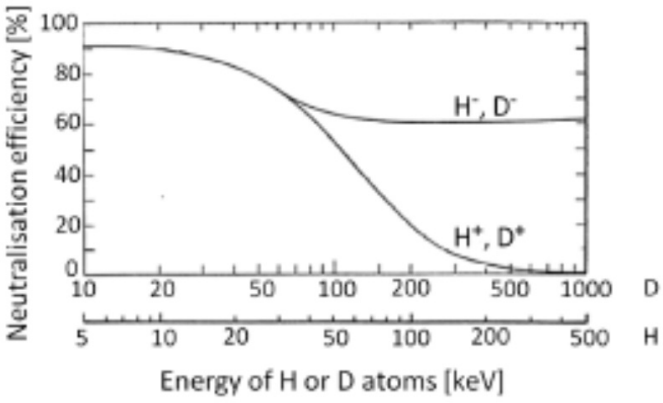

Figure 8: Neutralization efficiency of positive and negative ions as a function of their kinetic energy[1].

2 Processes in a negative ion source and physics of a particle beam

In this section, the structure of a negative ion source is described and an introduction on the beam physics is given.

2.1 Negative Ion Sources

In order to realize a negative ion source, firstly a gas is injected in the plasma chamber in a controlled way; secondly, a plasma is created through the collisions of accelerated electrons with the gas atoms. The simplest method to create such electrons is using a filament made of a material with an high atomic number (Tungsten or Molybdenum), operating as a cathode (*Arc Ion Sources (DC)*). The filament is heated until it starts to emit electrons by thermionic effect governed by the *Richardson's Law*:

$$j = AT^2 exp\left(-\frac{e\Phi}{k_B T}\right) \tag{9}$$

where A and k_B are constant, T is the filament temperature, e is the electronic charge and Φ is the work function, different for each metal.
Emitted electrons are then accelerated by the potential difference between the filament (cathode) and the chamber wall (anode), in which they create a plasma by ionization of the background gas. Arc Ion sources are simple but have some disadvantages: for example, an high impurity production into the plasma, moreover, because of sputtering, the filament has a finite lifetime, so it needs to be replaced frequently.
Considering this problem, for the ITER NBI source, the reference design is a Radio Frequency source (RF), the IPP RF source. In these sources (*AC sources*) an oscillating electric field is induced by a coil (*Inductively Coupled Plasma (ICP)*) which surrounds the plasma chamber. This field accelerates the free electrons in the source body, creating a plasma by ionization of the background gas.
Compared to arc sources, RF sources require less maintenance, since no filament is present.

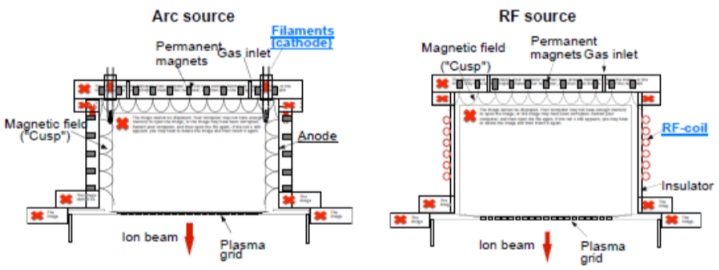

Figure 9: Representation of an Arc Ion source (on the left) and of a Radio Frequency source (on the right)[3]

Nevertheless, in both cases, the production of negative ions, H^- and D^-, takes place in the source through volume and/or surface processes, described in the next paragraph.

2.1.1 Creation of negative hydrogen ions H^-

The creation of negative hydrogen ions H^- can occur via volume or surface processes:

- Volume production: it is due to the dissociation of hydrogen molecules H_2 during collisions with electrons. This process happens in two steps: firstly H_2 molecules collide with high temperature electrons so that they are excited to an highly vibrational state $H_2(v)$; afterwards the latter collides with another electron at low temperature. The result of this collision is the unstable state H_2^-, which dissociates in H^0 and H^-. This two-step process is described by Eqs. (10) and (11).

$$H_2 + e^- \rightarrow H_2(v) + e^- \tag{10}$$

$$H_2(v) + e^- \rightarrow H_2^- \rightarrow H^- + H^0 \tag{11}$$

  where v indicates the vibrational excitation level and $H_2(v)$ is the excited hydrogen molecule, produced by the reaction in Eq. (10).

- Surface production: it is due to the interaction of hydrogen atoms and positive ions with the surface of the first grid of the extraction system, through which they are turned into negative ions, as shown in Eq. (12):

$$H, H^+ + e^-_{surface} \rightarrow H^- \tag{12}$$

  In the following figures the two processes are represented:

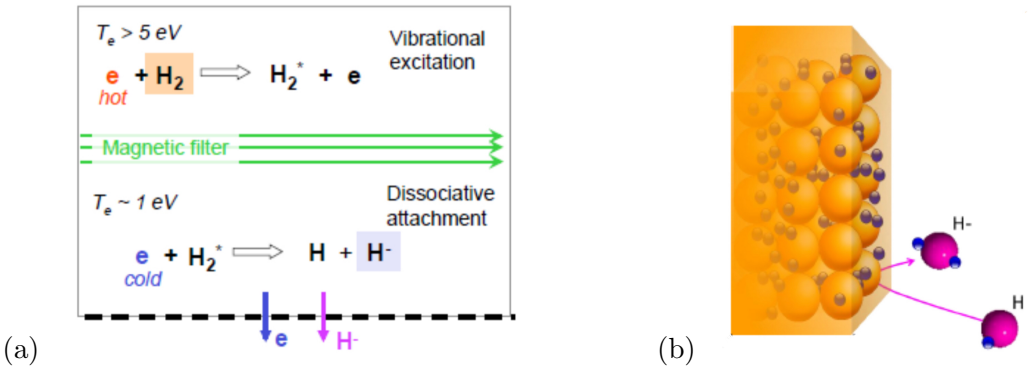

(a) (b)

Figure 10: (a) Representation of the volume production ; (b) representation of the surface production [3].

In a solid indeed, electrons are confined by the ionic charge and can not escape.
If Φ is the work function, i.e. the minimum binding energy of electrons in a solid, when the electron affinity E_a of an atom impinging onto the surface is higher than Φ, the probability that an electron is captured from the surface and a negative ion is formed is enhanced:

$$p \propto exp\left(\frac{E_a - \Phi}{v_\perp}\right) \tag{13}$$

where $v_\perp$ is the speed of the impinging atom perpendicular to the surface and E_a is the electron affinity (it is about 0.75 eV for ions H^-).
In the ITER negative ion source, the work function of the surface is maintained at a low value by covering the surface with Cesium. The latter, indeed, has the lowest work function (2.2 eV) and so, even using a small quantity, the negative ion yield considerably increases, as shown in the following graph:

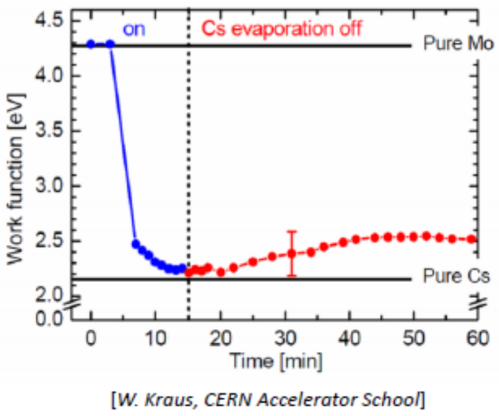

Figure 11: Graph of the work function Φ in time, with or without Cesium on the surface [3].

The volume processes permit to avoid the use of Cesium, whose distribution is governed by plasma and so it is difficult to predict. Nevertheless, the ratio between co-extracted electrons and hydrogen negative ions is high and the maximum extractable negative ion current density is quite low (< 50 A/m^2). Hence, it is recommended to use surface processes.
Being the binding energy of the additional electron of the H^- ion quite low, negative ions can be effectively destructed by various processes occurring within the source volume. The most relevant are:

- the mutual neutralization: $H^- + H^+ \rightarrow H + H$
- the electron detachment: $e^- + H^- \rightarrow 2e^- + H$
- the associative detachment: $H^- + H \rightarrow H + H + e^-$ or $H^- + H \rightarrow H_2 + e^-$

The reaction rate for the second process depends on the electrons temperature and it is dominant for $T_e \approx 2$ eV.
The production of negative ions presents thus opposite requirements. While hot electrons are needed to dissociate the H_2 molecules in the driver region, they are also destructive for the created negative ions. To separate the expansion region from the extraction zone near the PG, a magnetic filter field is established. Electrons, in fact, feel the magnetic field $\vec{B}$ and start to gyrate around the field lines following a trajectory of radius equal to the *Larmor Radius*:

$$r_L = \frac{mv_\perp}{|q|B} \tag{14}$$

where m, $v_\perp$ and q are the mass, the speed in the direction perpendicular to the magnetic field, and the electron charge, respectively.
However, electrons can pass the magnetic filter field in the axial direction through coulumbian collisions with a cross section σ_{Coul} depending on their velocity. The collision frequency ν_c is connected to the velocity by the relation Eq. (15):

$$\nu_c = n\sigma_{Coul}v \tag{15}$$

where v and n are the electron velocity and density, respectively. Consequently, since $\sigma_{Coul} \propto v^{-4}$, $\nu_c \propto v^{-3}$, so that the "cold" electrons are favoured to access to the extraction region.
The magnetic filter field near to the plasma grid, causes drifts in the plasma: the most important is given by the vectorial product $\vec{E} \times \vec{B}$ (where $\vec{E}$ is the electric field present in the plasma due to local variations of the plasma potential): $v_{\vec{E}\times\vec{B}} = \frac{\vec{E_\perp}\times\vec{B}}{B^2}$.
Mutual neutralization is the main destruction process of negative ions, downstream the magnetic filter field. Negative ions in the source, survive for a length of a few centimeters, therefore only the ions created near the plasma grid can be extracted.

2.1.2 The extraction region

The extraction and acceleration of negative ions occur through the use of 3 or more metal grids:

- the plasma grid (PG);
- the extraction grid (EG);
- the grounded grid (GG);

Each grid has many apertures, whose diameter usually varies in the range of 3-14 mm.
The interface between the plasma in the source and the vacuum of the accelerator, where charged particles feel the extraction potential, is called *meniscus*. It is generally identified as the surface at zero potential with respect to the source. Its area and shape mainly depend on the voltage of electrodes and on the plasma density, which is not usually constant. In general, the meniscus shape is a convex lens which determines the initial aiming of the beam particles.
For what concerns the plasma grid shape that optimizes the negative ion extraction, it appears that with a conic face, the acceleration force has a focusing component which forms a parallel beam at equilibrium. In planar geometry, the best inclination angle is identified as the *Pierce angle*, equal to 67.5°.
The extracted negative ions create some beamlets, passing through the apertures of the plasma grid (PG), and the total beam is given by all the beamlets exiting from the grids system.
The extraction grid (EG) is equipped with magnets that deflect the co-extracted electrons.

2.2 Beam physics

The optics characteristics of the beamlets, and consequently of the complete beam, depend on the spatial charge distribution and on the magnetic and electric fields of the extraction system.
An important parameter to describe the beam optics is the *perveance* P, defined as:

$$P = \frac{I_{ex}}{U_{ex}^{\frac{3}{2}}} \tag{16}$$

where I_{ex} and U_{ex} are the extracted current and the extraction voltage, respectively.
From the *Child-Langmuir Law* it is possible to obtain the maximum extractable current I_{ex}^{max} (Eq. (17)) and a maximum perveance P_0 (Eq. (18)):

$$I_{ex}^{max} = \frac{4}{9}\pi\epsilon_0\sqrt{\frac{2Ze}{m}}\left(\frac{r}{d}\right)^2 U_{ex}^{\frac{3}{2}} \tag{17}$$

$$P_0 = \frac{I_{ex}^{max}}{U_{ex}^{\frac{3}{2}}} = \frac{4}{9}\pi\epsilon_0\sqrt{\frac{2Ze}{m}}\left(\frac{r}{d}\right)^2 \tag{18}$$

where ϵ_0, Z, e, m, r and d are respectively the permittivity of the vacuum, the state of ionic charge, the electron charge, the particle mass, the aperture radius and the distance between the plasma grid and the extraction grid. Consequently, P_0 depends only on the grid characteristics and on the effective mass of the ion species.
As a reference parameter to describe the beam optics, it is usually used the *normalized perveance* $\frac{P}{P_0}$. It is correlated with the beam divergence, which is an index of the beamlet opening caused by the spatial charge expansion. The divergence is defined as a measure of the width of the velocity distribution in the plane transverse to the direction of beam propagation. Generally, the distribution of the angles between the beam axis and the velocity vector of the beam particles is well described by a *Gaussian distribution*[2] with standard deviation σ, consequently the divergence is assumed as the 1/e width of that Gaussian.

[2]Gaussian distribution: $\frac{1}{\sigma\sqrt{2\pi}}e^{-\frac{(x-m)^2}{2\sigma^2}}$

In general, the beam divergence angle ϵ depends on the perveance (and consequently on the extracted current and the extraction voltage) and on the ratio between the acceleration and extraction potential (see Eq. (19)):

$$\epsilon = \epsilon \left(\frac{P}{P_0}, \frac{U_{acc}}{U_{ex}} \right) \tag{19}$$

The condition of minimum beam divergence is called optimum normalized perveance: with increasing the ratio $\frac{P}{P_0}$, the divergence decreases (under-perveant region) until it reaches its minimum, then it increases again (over-perveant region).
The extraction system can be considered as an electrostatic lenses system: the normalized perveance is linked to the focal point of the single beamlet. This explains why a bad optics is correlated to a large divergence, as shown in Fig. 12.

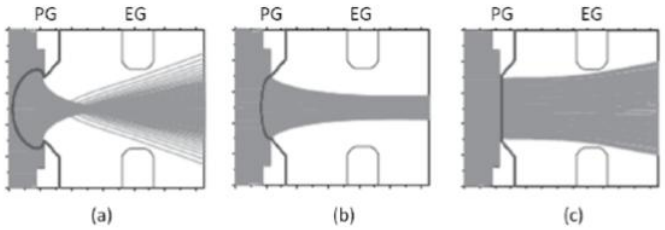

Figure 12: Illustration of the beamlet shape in three different cases: in case (a) and (c) the beam optics is bad (big broadening). In case (b), instead, the focal point is near the EG but far enough to succeed in obtaining a good optics [26].

The repulsive electrostatic force due to the negative charge of the beamlets, causes a continue increase of their divergence. Nevertheless, in the drift region, the beam interacts with the background gas. The plasma generated in this interaction, as described in the *Introduction*, can shield the potential of the beam itself, limiting its enlargement. The main reactions happening in the drift region are the following:

- Ionization of H^0: $H^0 + H_2 \rightarrow H^+ + e^- + H_2$
- Ionization of H_2: $H^0 + H_2 \rightarrow H^0 + e^- + H_2^+$
- Double stripping of H^-: $H^- + H_2 \rightarrow H^+ + 2e^- + H_2$

The creation of positive ions H^+ generates an attractive electrostatic force which reduces the beamlets broadening.
Since the negative hydrogen ions have a very low binding energy (0.75 eV), they can easily be neutralized through collisions with the residual gas. The neutralization occurs not only in the drift region, but also in the extraction region before they reach their full energy. In this case, the neutral particle obtained, is useless for plasma heating since it can no longer be accelerated by the electric fields in the accelerator and consequently it proceeds with a wrong trajectory without reaching the tokamak.
The stripping process (the loss of an electron), strongly depends on the gas pressure. Therefore, the pressure needs to be optimize in order to minimize the stripping losses. For example, for the ITER NBI system, a source with a pressure below 0.3 Pa is required. At this pressure, the stripping losses are assumed to be about 30 %.
For a negative hydrogen ion beam, there are two stripping reactions:

- Stripping of H^-: $H^- + H_2 \rightarrow H^0 + e^- + H_2$
- Double stripping of H^-: $H^- + H_2 \rightarrow H^+ + 2e^- + H_2$

The fraction of surviving beam particles, for which the stripping process did not occur (unstripped particles), can be calculated by a 1D model, considering the density profile of neutral particles $n(x)$,

which can be obtained from measures of gas pressure and local temperature along the beamlet axis:

$$f_s(x_{GG}) = exp\left(-\int_{x=0}^{x=x_{GG}} n(x)\cdot\sigma_{strip}(E(x))dx\right) \tag{20}$$

where x_{GG} is the grounded grid (GG) position, assuming that the origin of the beamlet axis is the plasma grid (PG) position; σ_{strip} is the stripping cross section and it depends on the local particle energy $E(x)$. Therefore, the stripping losses mainly depend on two factors: the particle energy (hence on the extraction and acceleration voltage) and the source pressure (since the stripping losses are correlated to the neutral density profile, as shown in Eq. (20)).

3 The negative ion source SPIDER and the STRIKE calorimeter

In the following section, the negative ion source SPIDER (***S**ource for the **P**roduction of **I**ons of **D**euterium **E**xtracted from a **R**adio Frequency plasma*) and the diagnostic calorimeter STRIKE (***S**hort-**T**ime **R**etractable **I**nstrumented **K**alorimeter **E**xperiment*) are described.

3.1 The ion source SPIDER

The test facility SPIDER was built at Consorzio RFX in Padova (Italy), in order to study and optimize negative ion production for the ITER neutral beam injectors. SPIDER is a negative ion source providing an expected beam energy of 100 keV and a current intensity of about 50 A. The required parameters are summarized in Tab. 4:

SPIDER requirements	H	D
Beam energy	100 keV	100 keV
Max beam source filling pressure	0.3 Pa	0.3 Pa
Max deviation from uniformity	$\pm 10\%$	$\pm 10\%$
Current density of ions extracted from the plasma	> 355 A/m^2	> 285 A/m^2
Beam on time	3600 s	3600 s
Co-extracted electron fraction (e^-/H^-) and (e^-/D^-)	< 0.5	< 1

Table 4: SPIDER requirements [7]

The SPIDER Vacuum Vessel (VV) consists of a stainless steel (AISI 304 L) cylindrical chamber, having diameter of 4 m and an overall length of about 6 m.
The most complex part of SPIDER, the Beam Source (BS), consists of plasma source and extractor. It has the same size and characteristics of the ITER beam source.
The plasma is created inside eight small cylindrical chambers, called *drivers*, in which an hydrogen or deuterium gas is injected at a pressure of about 0.3 Pa. There it is ionized by RF power transferred from coils wound around the drivers [7]. After that, plasma diffuses inside an expansion chamber towards the plasma grid (PG), which is usually covered with a layer of cesium in order to reduce the work function and thus increase the negative ion production. Nevertheless, during the first phase of experimental activity, cesium is not used.
In order to decrease the electron density in front of the extraction apertures, a bias plate (BP) with adjustable potential, is mounted 10 mm upstream of the PG. Hence, it is possible to modify and optimize the electric field distribution in the region of negative ion production, in order to reduce the co-extracted electrons. Indeed, it is necessary to minimize the acceleration of the latter in order to avoid overheating of the grids and to reduce power loss.
Between the PG and the following grid (the extraction grid, EG) a potential difference U_{ex} is applied so that the negatively charged particles are extracted from plasma through the PG apertures. The grids, about 2 m^2 wide (approximately 1600 mm high and 800 mm wide), are provided with 1280 apertures: the overall beam is thus constituted by 1280 beamlets, subdivided into 4 $\times$ 4 groups of 5 $\times$ 16 beamlets each. The grids are also divided into four segments for alignment and manufacturing reasons, as shown in Fig. 14(b).
The electrons which are extracted together with the negative ions are dumped onto the EG by a magnet system ("suppression magnets") located in the EG itself. The negative ions are then accelerated by an acceleration potential U_{acc} applied between the EG and the GG. An illustration of the SPIDER grid system is given in Fig. 13.

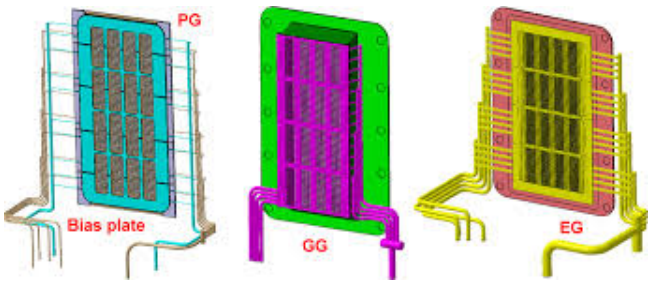

Figure 13: Illustration of the SPIDER grid system for the negative ion extraction and acceleration [14].

The SPIDER design, shown in Fig. 14(a), aims to obtain the best beamlet optics, considering both the physics and engineering aspects. For this purpose, the aperture shape and the distances between the grids were optimized in order to steer the beamlets and to counteract the electrostatic repulsion among them (see Fig. 14(c)).
Moreover, in order to reduce the local density and temperature of electrons in the plasma near the PG, a horizontal magnetic filter field is used. It is generated by a current, I_{filter}, flowing in the vertical direction inside the plasma grid itself. Furthermore, an electron dump (ED), constituted of a series of vertical pipes, has been added downstream of the GG, in order to discard the electrons exiting from the accelerator.

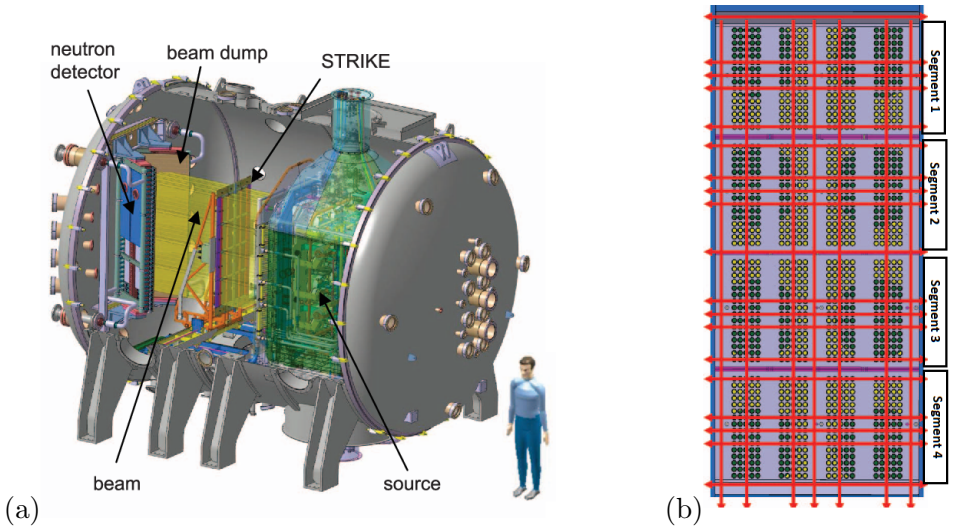

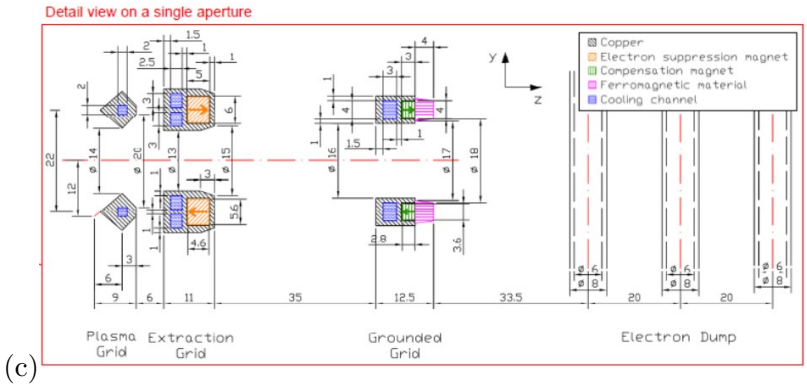

Figure 14: (a) Design of the SPIDER negative ion source; (b) illustration of the 1280 beamlet apertures, with the segment divisions [8]; (c) vertical section of the SPIDER extractor/accelerator system and electron dump (all the dimensions are in mm) [27] .

The magnetic field which dumps electrons on the EG, also affects negative ions trajectories. The GG compensates for the beamlet deflections inside the accelerator, as described later in Sec.4.2.

The experimental data obtained by SPIDER operation, are extremely important for the source and beam characterization. For this reason, SPIDER is provided with many diagnostics, summarized in the following Table:

Source Diagnostics	Beam diagnostics
Electrical currents	Calorimetry and surface thermocouples (beam uniformity, divergence, aiming)
Calorimetry and surface thermocouples (powerload on source components)	Instrumented calorimeter STRIKE (detailed layout of STRIKE given in Sec.3.2)
Electrostatic probes (plasma uniformity, T_e, n_e)	Beam emission spectroscopy (BES) (beam divergence and uniformity, stripping losses)
Source optical emission spectroscopy (OES) (T_e, n_e, n_{H^-}, n_{cs}, n_H, impurities)	Beam tomography (beam uniformity over 2D profile, resolution 1/4 beamlet group)
CRDS (n_{H^-}), laser absorption (n_{Cs})	Neutron imaging (beam uniformity horiz. profile, resolution 3-4 cm, D only)

Table 5: SPIDER diagnostics [7]

SPIDER is provided with two calorimeters: the water-cooled Beam Dump (BD) and the high-spatial-resolution uncooled calorimeter STRIKE (see Sec. 3.2)[7]. The first can absorb a maximum power of 6 MW and it is made of two panels arranged in a V shape at 60°, so that the beam incidence angle is about 30°. Nevertheless this calorimeter can only provide low resolution information on the beam uniformity and divergence; hence, STRIKE is necessary to integrate the calorimetric estimates of the parameters measured by BD.
For what concerns the Power Supply (PS) system, it includes the Ion Source and Extraction Power Supply (ISEPS) and the Acceleration Grid Power Supply (AGPS). As the ion source operates at -100 kV with respect to ground, ISEPS is situated in a large Faraday cage (of size: 13m × 11 m × 5 m), called *High Voltage Deck* (HVD) [7]. In order to reduce the electromagnetic interference (EMI), HVD is clad with a conductive metal sheet and it is mounted on supporting insulators.

3.2 The diagnostic calorimeter STRIKE

In order to reach the high temperatures necessary for thermonuclear fusion in ITER experiment, additional heating systems are needed, such as the injection of neutral beams from accelerated negative ions; in particular two injectors (NBI) will deliver a total power of 33 MW. Among the characteristics of ITER neutral beam Injectors, beam uniformity within ±10% is required [21]. The STRIKE calorimeter is a diagnostic instrument whose aim is to characterize the SPIDER negative ion beam during short pulse operation, in order to obtain a good knowledge of the beam characteristics. The most relevant measurements performed by STRIKE are: beam uniformity and current, beamlet divergence and deflection, and stripping losses.
STRIKE is made of 16 one-directional (1D) Carbon Fiber Composite (CFC) tiles, dimensioned to accommodate a single beamlet group. The full beam produced in the source, indeed, is subdivided in 4×4 groups of $5(horizontally) \times 16(vertically)$ beamlets each. The 16 tiles are organized in two panels of 8 tiles each, perpendicular to the beam. Since a radiative sheet is expected to form in front of the calorimeter, tiles are observed by thermal cameras on the rear side. Therefore, the tile material must maintain on the rear side a beamlet footprint as similar to the front one as possible [21]. For this purpose, the 1D-CFC material has been studied and selected for its particular properties, such as the high ratio between thermal conductivity in the direction parallel to the beam and those in the directions perpendicular to the beam.
The STRIKE design is shown in Fig. 15:

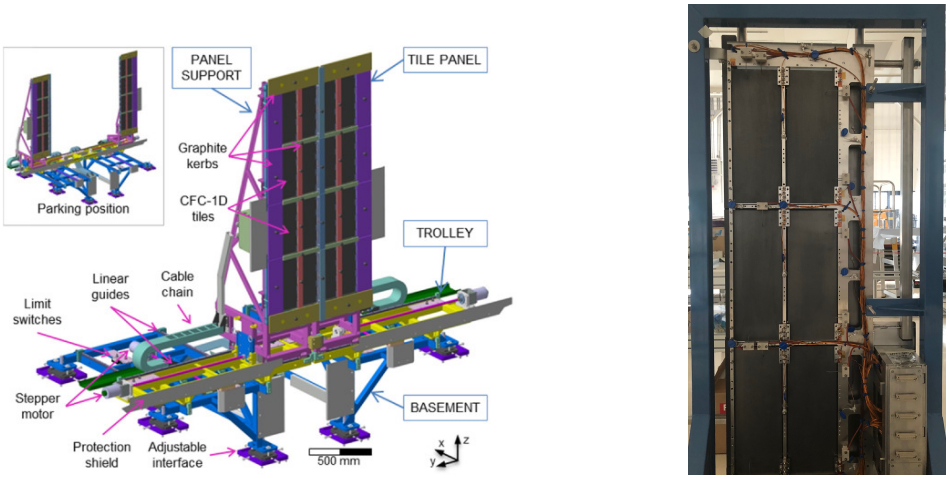

Figure 15: (a) Illustration of STRIKE with its supporting and positioning system [7]; (b) Picture of the STRIKE left panel (only six tiles are shown).

3.2.1 1D-CFC Tiles

The requirements of 1D-CFC (Carbon matrix-Carbon Fibre reinforced Composite) material include:

- a large thermal conductivity along the tile thickness (at least 10 times larger than in the other directions);
- a low density and specific heat;
- uniform parameters over the tile surface;
- capability to withstand localized heat loads;

Therefore 1D-CFC is an extremely anisotropic and delicate material, not commercially available. So, specific prototypes were realized and tested in the last years, aiming at valuing the uniformity and temperature dependence of the thermal parameters, and at verifying the thermo-mechanical resistance of the tiles, irradiated by a huge localized energy flux. The prototypes which satisfied the requirements, were successfully employed in different ion source test facilities, such as BATMAN (IPP, Garching) [10], NIFS-RNIS (Tokio, Japan) [15] and NIO1 (Padova, Italy) [19]. The prototypes dimensions, however, were smaller than the current STRIKE tiles ($376 \times 142 \times 20$ mm^3)[20]. Hence, a full size prototype, has been later realized and tested. A visual inspection of these tiles reveals many localized defects on their surface, some of them are shown in Fig.16(b) [12]. The picture of two STRIKE tiles is shown in Fig. 16(a).

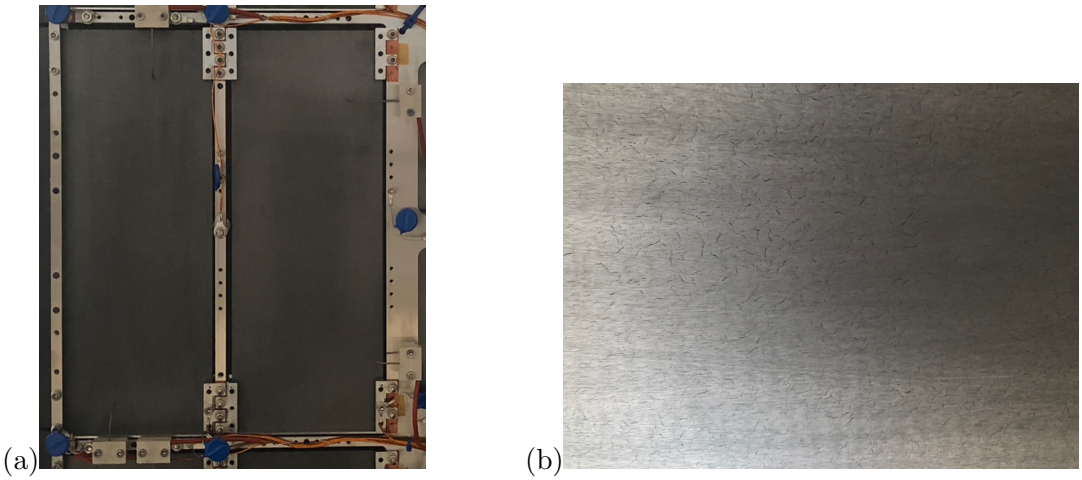

Figure 16: (a) Picture of two tiles of STRIKE; (b) details of the tile surface.

The definitive tiles were also tested and they seemed to verify the required parameters, in particular the ratio between the conductivities is about 20. Moreover, from the analysis of the prototypes and of the definitive tiles, an estimate of the *thermal emissivity* is given: it results equal to $\epsilon = 0.85$ (which is also the value used in the codes for the data analysis).

3.2.2 STRIKE diagnostics

The diagnostics dedicated to the STRIKE calorimeter are:

- two infrared (IR) cameras (i.e. thermal cameras) to measure the changes of temperature;
- thermocouples to calibrate the thermal cameras throughout a local temperature measurement;
- current sensors to measure the current associated to the particle beam;
- electrostatic sensors to characterize the plasma formed by the interaction of the beam with the background gas;

The main diagnostics to characterize the ion beam are the IR cameras, which measure the 2D map of the temperature of the entire beam cross section with a spatial resolution less than 2 mm, an acquisition frequency higher than 25 frames/s, and an accuracy of the axial positioning of $\pm$ 5 mm. In this way, the error induced by the beamlet pattern can be limited below $\pm 5\%$, so that it is possible to recognize with a sufficient confidence whether the beam non-uniformity is within 10%. Hence, the two thermal cameras, located on the SPIDER vessel (one at the top and one at the bottom), are used to observe the rear side of the STRIKE tiles through dedicated windows. These cameras have a display of 640×480 pixels to satisfy the spatial coverage and resolution requirements. The part of the calorimeter that each thermal camera can observe, is shown in Fig. 17. In both cases, all points are seen at an angle to the surface $\geq 30°$, condition necessary to have reliable temperature measurements [21].

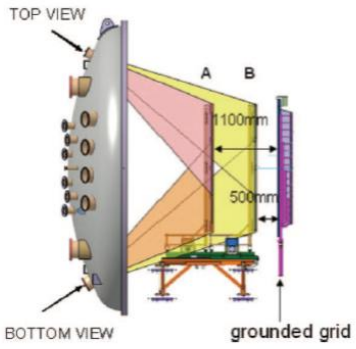

Figure 17: Illustration of the STRIKE positions for the measurements (A e B) and portions observed by IR cameras [21].

Referring to the Fig.17, when STRIKE is in position A, at 1100 mm from the GG, the middle point is at 2280 mm from the thermal camera and the surface is seen at an incidence angle of 35° with respect to the normal plane. Whereas, in position B, at only 500 mm from the GG, the middle point is at 2800 mm from the camera and the surface is seen at an incidence angle of 30° with respect to the normal [21].

The STRIKE thermocouples require many features for diagnostic scopes: they must be vacuum compatible (at a pressure of about $P = 10^{-3}$ Pa); they must operate in the presence of RF waves and x rays. Moreover, a good sensitivity to temperature changes, repeatability of the measurements and sufficient linearity over the relevant temperature range are required. Hence , a type N of thermocouples was selected [23]. For the calibration of the IR cameras, two thermocouples are located on the rear

side of the tiles: one is on the edge of the tile (for a "*cold reference*") and one is in correspondence to a beamlet (for a "*hot reference*").

As a supplement to the measurements of the beam non uniformity, the current flowing into each tile is measured. The current sensors can measure a current intensity up to 5 A with 12 bit resolution.

Two electrostatic sensors for each panel are positioned, as shown in Fig. 18(b):

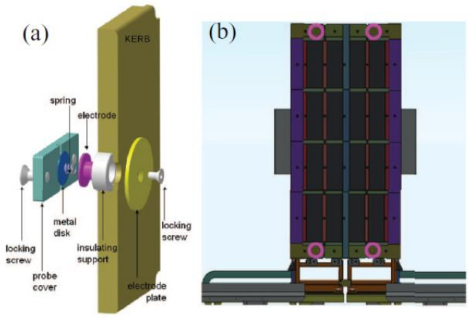

Figure 18: View (a) and position (b) of the STRIKE electrostatic sensors [21].

Impact of ions and neutrals on material surfaces induces the emission of secondary electrons which can affect the measurement of the beam current[3]. Hence, it is necessary to positively bias the STRIKE surfaces with respect to the grounded grid, so that the secondary electrons are always re-absorbed on the same tile they were emitted from. During the first phase of experimental activity, tiles were biased at 60 V.
In the first phase of experimentation, only the STRIKE right panel (seen by the impinging beam) was installed. It is composed of 8 tiles, numbered as shown in Fig. 19:

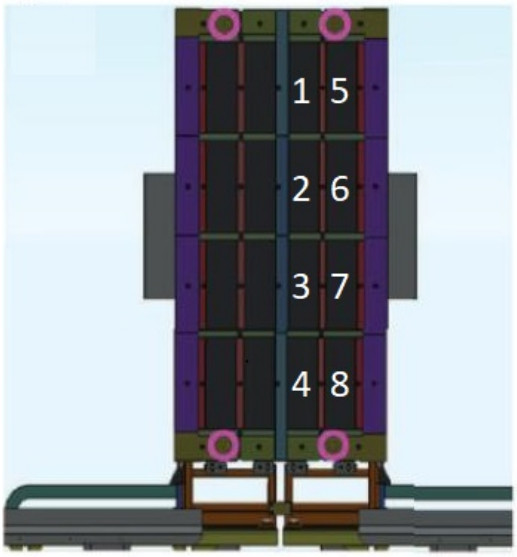

Figure 19: Visualization of the STRIKE right panel, with numbering.

[3]The coefficient of secondary emission depends on both the type of projectile and target; e.g. for a hydrogen beam of 100 keV on a graphite target, the coefficient is equal to 2.55

4 Software for the Data Analysis of STRIKE

In this section, the programs used to analyze STRIKE data are illustrated.
The programming language used for developing the data analysis software is MATLAB.
The tiles of the STRIKE right panel are observed by two thermal cameras (of 640 × 480 pixels), each of which can examine only 6 tiles; in particular, referring to Fig. 19, the camera at the top (called "*cam 1*") sees the temperature increase on tiles #1, #2, #3, #5, #6, #7, whereas the camera at the bottom ("*cam 2*") observes tiles #2, #3, #4, #6, #7, #8. Hence, it was chosen to develop two programs, one for each camera, exactly identical for what concerns the effected analysis. The procedures of the code will be accurately explained, by taking as example the pulse #6043, whose operational parameters are summarized in the following Table:

Parameters	Value
Filter current I_{filter}	1.5 kA
Extraction voltage U_{ex}	2 kV
Acceleration voltage U_{acc}	20kV
RF Power	80 kW/gen
Electronic current I_{EG}	11.7 A
AGPS current I_{AGPS}	0.37 A
Pulse duration Δt	13.5 s
Acquisition frequency	1 frame every 0.52 s

Table 6: Parameters of the reference pulse #6043

4.1 First analysis

After loading all the frames of the analyzed shot and converting the data of the thermal camera from radiometric to Celsius, a series of steps are carried out:

- Determination of the pulse start and stop:
  the simplest way to find the first frame of the beam-on phase, is to determine when the temperature of the tiles, hit by the beam, starts to increase. In particular, a threshold is fixed (of 0.03 K for the examined pulse), and the first frame with a temperature difference higher or equal to the threshold one, is considered as the starting frame. For the pulse end, an analogous procedure is followed: the frame in which the temperature difference with the previous frame, goes below the fixed threshold, is considered as the beam ending frame. Moreover, the program finds the segment where the beam starts, by choosing the first segment where an increase of temperature is detected. In fact, this separation of segments, was due to three main reasons:
  - firstly, tiles are actually separated and we were looking for the beamlets where the greatest temperature increase was registered;
  - in some pulses not all the RF generators were used, consequently there were segments without beam signal;
  - if there is a low signal, since beam is not uniform (see Sec. 5.1), the fixed threshold can be exceeded only on certain segments;

  For the pulse #6043 the beam-on phase starts at frame 89 on segment #1 and ends at frame 115.
  In addition, the average temperature T_{avg} and the maximum temperature T_{max} are calculated on each tile seen by the thermal cameras. In Fig. 20 the average temperature time trace are shown:

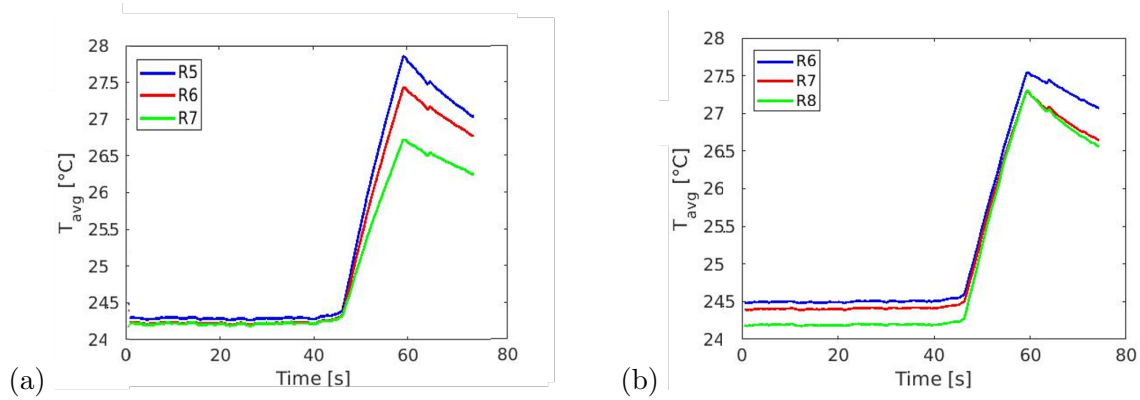

Figure 20: (a) Average temperature time trace on tiles #5 (blue), #6 (red), #7 (green) seen by *cam 1*; (b) average temperature time trace on tiles #6 (blue), #7 (red), #8 (green) seen by *cam 2* of pulse #6043.

The two graphics above show a similar trend: temperature is constant for about 45 s from the beginning of the shot, and then it rapidly increases as the beam starts. The beam-on phase lasts few seconds and at the end of it, temperature decreases, as expected. This can also be seen by the voltage and current signals given by the acceleration grid power supply (AGPS), shown in the following figure:

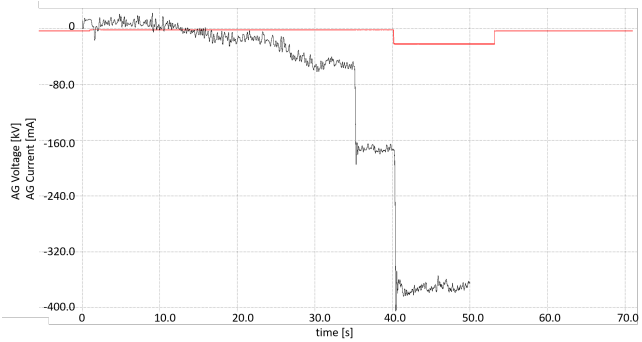

Figure 21: Acceleration voltage (red) and ionic current (black) time trace measured by the AGPS for pulse #6043.

- Background subtraction:
  once the first frame of the beam-on phase is found, the profile of the background temperature can be evaluated by taking into consideration the average of the ten frames before the starting frame. Thus, this background is subtracted from each frame of the beam-on phase.
  The images of the IR camera on the bottom, *cam 2*, corresponding to the raw data, the background data and the temperature increase (i.e. the difference of the raw and the background data) are shown in Fig. 22.

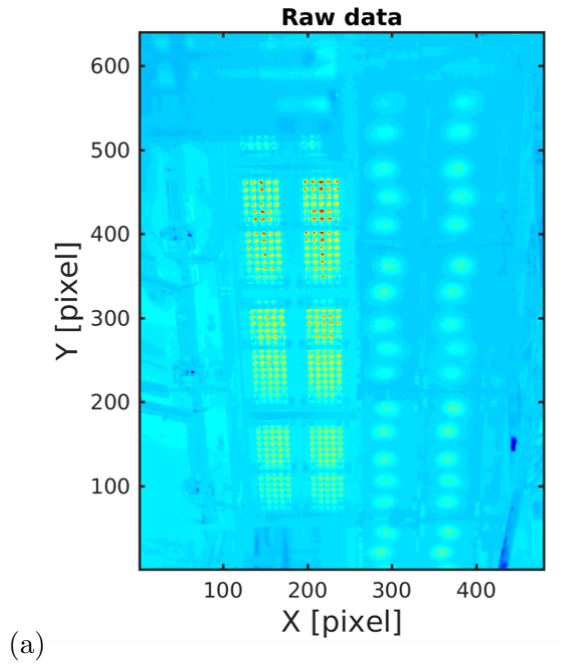

(a)

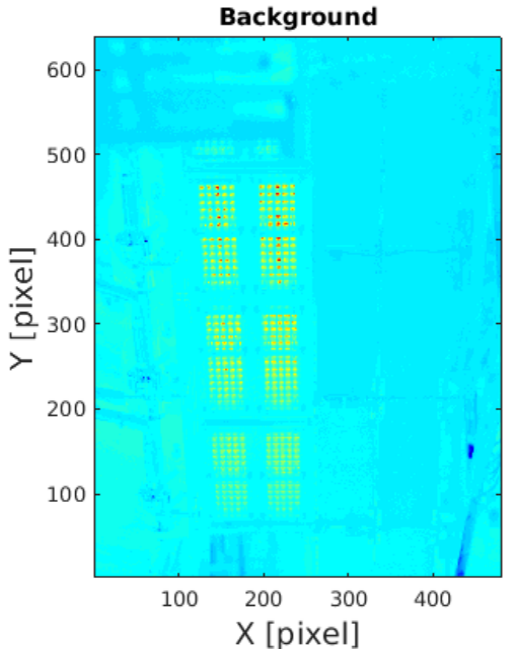

(b)

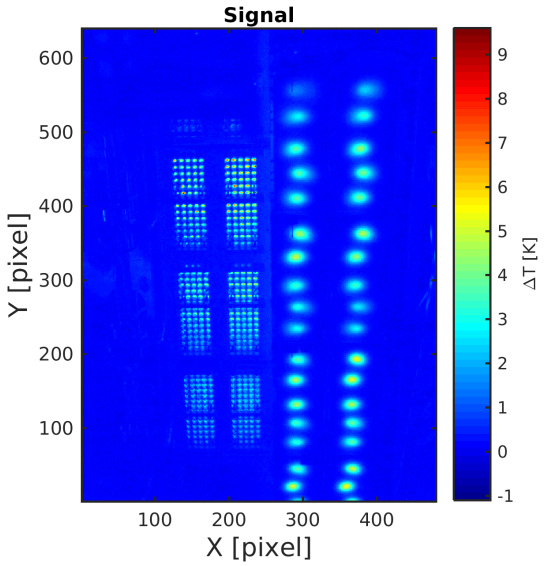

(c)

Figure 22: (a) Image of raw data at t=5.2 s after the onset of beam; (b) Image of the background data: average of the ten frames before the onset of beam; (c) image of the temperature increase at t=5.2 s after the onset of beam, for the pulse #6043 seen by *cam 2*.

- Image clipping:
  in the left half of Fig. 22 the Grounded Grid (GG) is shown. Therefore, the right part of the matrix forming the image, is selected, in order to visualize only the STRIKE right panel, as shown in the following figures:

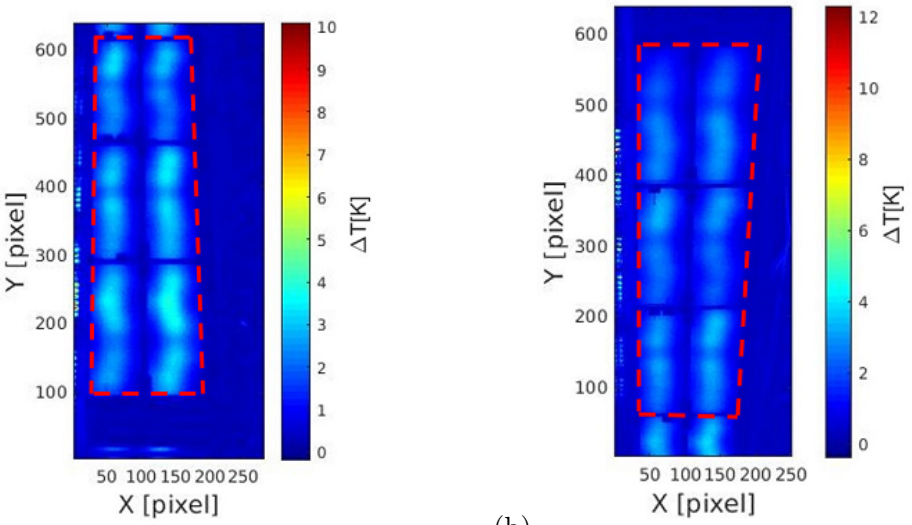

Figure 23: (a) Image clipping seen by *cam 1* at the last frame of pulse #6043; (b) image clipping seen by *cam 2* at the last frame of pulse #6043.

- Perspective correction:
  since the thermal cameras observe the tiles at an angle $\geq 30°$, it is necessary to correct the geometrical perspective of the original image. First of all, the vanishing point needs to be found; this is obtained as the meeting point of the two lines corresponding to the long sides of the STRIKE panel. The perspective is then corrected moving on a vertical line the elements belonging to a line passing through the vanishing point. In particular, in the program, a homographic transformation is used: the entering and exiting points are given in input, by considering the vertices of the trapezoid formed by the STRIKE panel (as underlined by the dashed red lines in Fig. 23), obtaining in output a matrix that maps the ones in the others (SVD method [18]).
  After that, the image resulting from the perspective correction, is flipped from up to down and mirrored from right to left in order to obtain the correct image seen by thermal cameras.
  The resulting figures are displayed in Fig. 24.

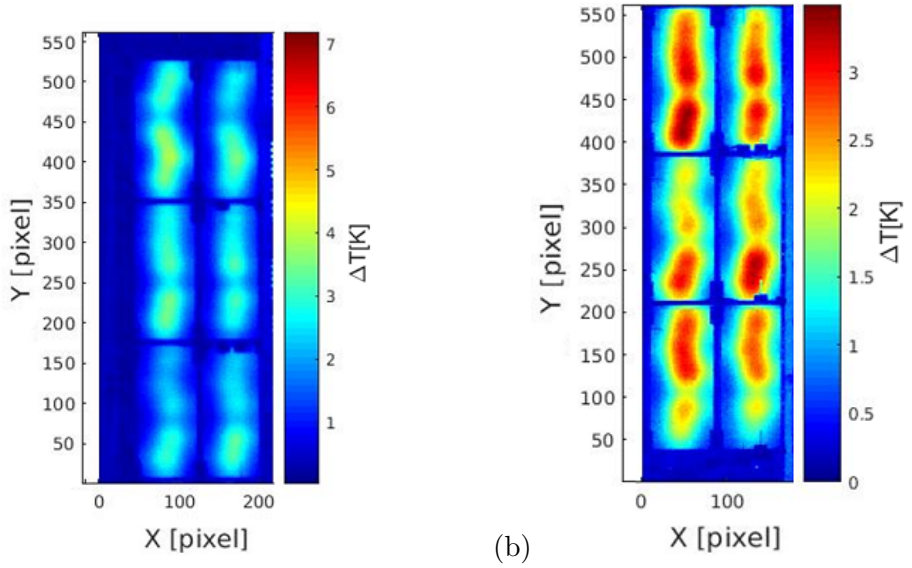

Figure 24: (a) Image corrected seen by *cam 1*; (b) image corrected seen by *cam 2* at the last frame of pulse #6043.

After the perspective correction, the pixel to millimeter conversion is obtained: the multiplication factors (horizontal for x axis and vertical for y axis) are calculated by taking into consideration the real dimensions of the tiles, compared to their dimensions in pixel in the image given by the IR camera.

- Computation of the energy deposited on each tile:
  From the previous image, the regions corresponding to each tile are selected, and for each of them, the temperature values at the beginning and at the end of the beam-on phase ($T_{background}$ and T_{end}) are found. In this way, it is possible to calculate the temperature increase ΔT as the difference among them. Then, by knowing the tile density ρ, volume V and specific heat c, the energy deposited on each tile by the impinging particle beam is obtained as:

$$E_{cal} = c\rho V \Delta T \tag{21}$$

  The temperature increase seen by *cam 1* and *cam 2* on tiles is shown in Fig. 25.

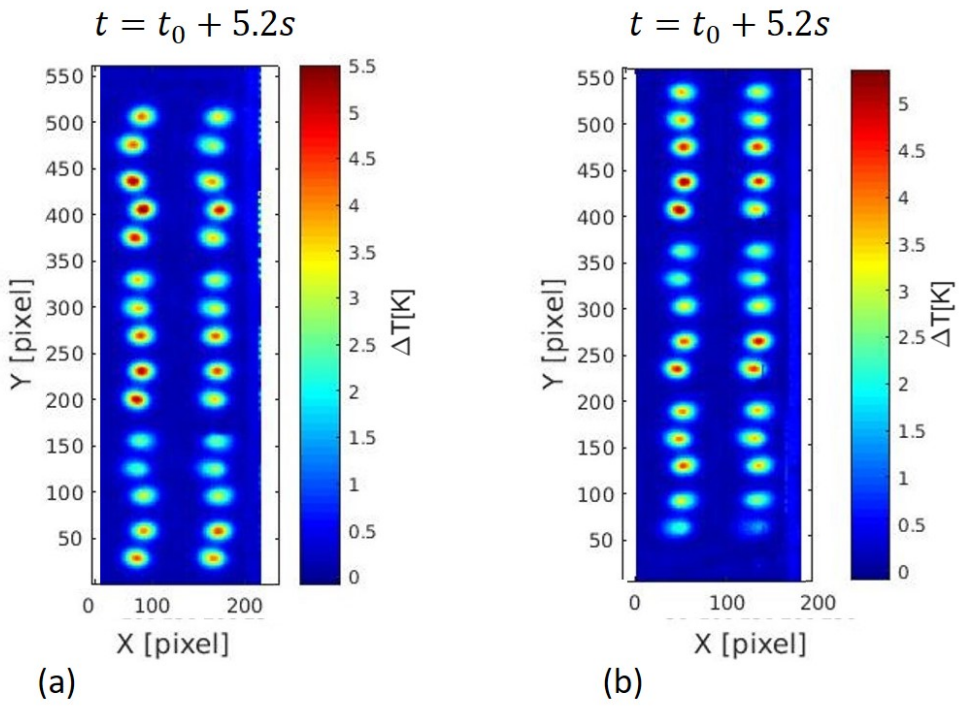

Figure 25: (a) Temperature increase on Tiles seen by *cam 1*; (b) temperature increase seen by *cam 2*, of pulse #6043 at frame 10 (i.e. t= 5.2 s after the onset of the beam).

- 2D Gaussian Fit:
  for the regions corresponding to each tile, previously selected, an experimental data fit is executed through a 2-dimensional Gaussian function. In particular, since on each tile 5 peaks, corresponding to the impinging beamlets (more details in Sec. 4.2), are observed, the fitting function is given by the sum of five Gaussian curves:

$$G(x,y) = \sum_{i=1}^{5} A_i e^{-\left(\frac{x-x_{c_i}}{w_{x_i}}\right)^2} e^{-\left(\frac{y-y_{c_i}}{w_{y_i}}\right)^2} \tag{22}$$

  From this fit, for the ten frames after the starting frame, the following parameters are deduced: the centre coordinates (x_{c_i}, y_{c_i}), the widths (w_{x_i}, w_{y_i}) and the normalization constants A_i of the i-th peak.
  The temperature profiles of the measured data, the fit and the residuals (i.e. the difference between data and fit) of tiles seen by *cam 1* are shown in Fig. 26, 27, 28, 29, 30, 31:

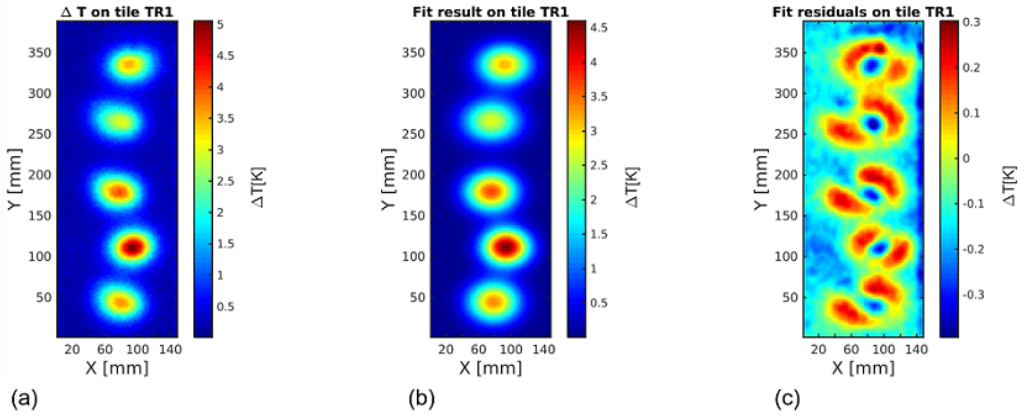

Figure 26: (a) Temperature profile of the measured data;(b) temperature profile given by the fit;(c) Residuals profile (i.e. the difference between data and fit) of the pulse #6043 at t=5.2s after the onset of the beam on tile #1 seen by *cam 1*.

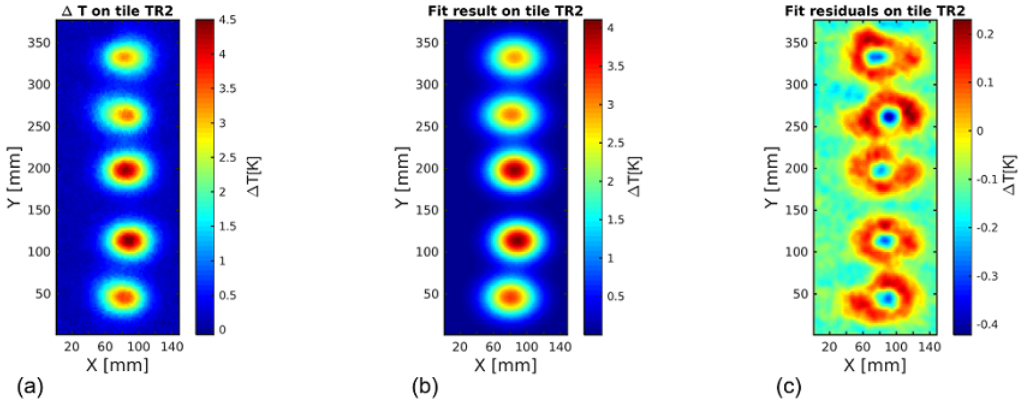

Figure 27: (a) Temperature profile of the measured data;(b) temperature profile given by the fit;(c) Residuals profile (i.e. the difference between data and fit) of the pulse #6043 at t=5.2s after the onset of the beam on tile #2 seen by *cam 1*.

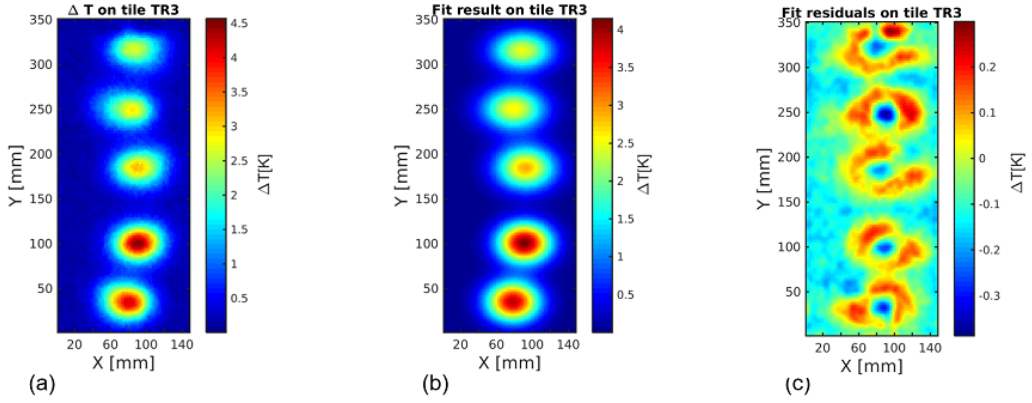

Figure 28: (a) Temperature profile of the measured data;(b) temperature profile given by the fit;(c) Residuals profile (i.e. the difference between data and fit) of the pulse #6043 at t=5.2s after the onset of the beam on tile #3 seen by *cam 1*.

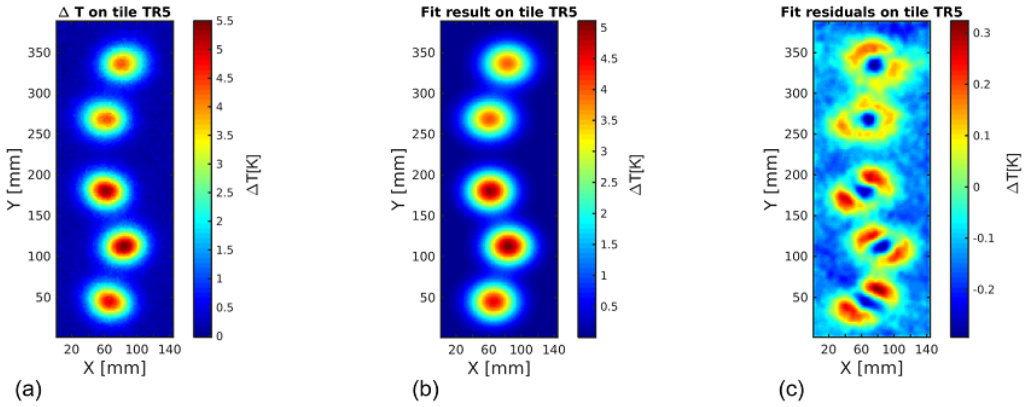

Figure 29: (a) Temperature profile of the measured data;(b) temperature profile given by the fit;(c) Residuals profile (i.e. the difference between data and fit) of the pulse #6043 at t=5.2s after the onset of the beam on tile #5 seen by *cam 1*.

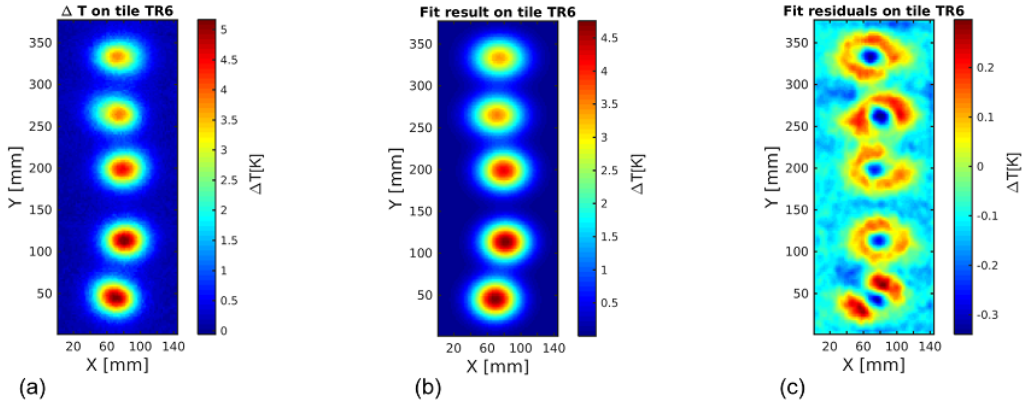

Figure 30: (a) Temperature profile of the measured data;(b) temperature profile given by the fit;(c) Residuals profile (i.e. the difference between data and fit) of the pulse #6043 at t=5.2s after the onset of the beam on tile #6 seen by *cam 1*.

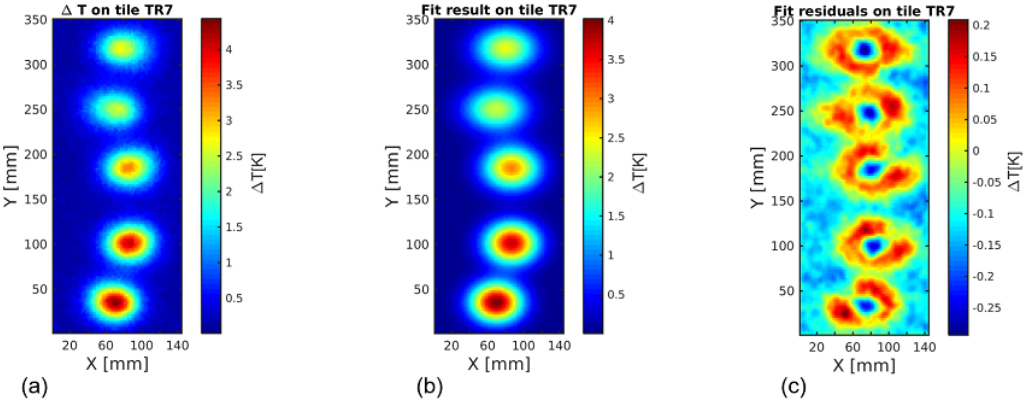

Figure 31: (a) Temperature profile of the measured data;(b) temperature profile given by the fit;(c) Residuals profile (i.e. the difference between data and fit) of the pulse #6043 at t=5.2s after the onset of the beam on tile #7 seen by *cam 1*.

Looking at the residuals profile of the figures above, it can be noticed that the temperature difference is very low (the maximum is about 10% of the measured data), which means that the fit results succeeded relatively well. Nevertheless, by comparing figures of measured data (Fig. 26(a), 27(a), 28(a), 29(a), 30(a), 31(a)) with their respective figures resulting from fit (Fig. 26(b), 27(b), 28(b), 29(b), 30(b), 31(b)), it can be observed that the shape of the measured data is not exactly a horizontal ellipse, but rather they seem to be ellipses with a particular orientation angle which is not considered in the fitting process. This is the reason why the residuals profile (Fig. 26(c), 27(c), 28(c), 29(c), 30(c), 31(c)) appears quite correlated to the shape of the original data.

- Creation of the structure called *Tiles*:
  finally, the structure "*Tiles*" is created. It contains many parameters, available for further analysis, such as the *Post processing* (see Sec. 4.2). Among the substructures of Tiles, there are: the multiplication factors for the pixel to millimeter conversion, the starting and the ending frame of the beam-on phase, the average temperature T_{avg}, the fit parameters for the ten frames after the beginning and a vector containing the energy deposited on each tile. The latter are reported for pulse #6043 in Tab. 7 in Sec.4.2.

4.2 Post Processing analysis

Starting from the parameters of the structures *Tiles1* and *Tiles2*, respectively produced by the data of the thermal cameras *cam 1* and *cam 2* in the first analysis (see Sec. 4.1), other relevant physical quantities are calculated.
Since tiles $\#2, \#3, \#6, \#7$ are observed by both *cam 1* and *cam 2*, for these tiles there were two estimates of all the analyzed physical quantities. Hence, in the data analysis of these tiles, an average of the two estimates was calculated.

- Calorimetric Current I_{cal}:
  by dividing the deposited energy on each tile for the pulse duration Δt, the power P is deduced. Hence, upon dividing again the latter for the average acceleration potential U_{acc}, the average current flowing on each tile, is found as:

$$I_{cal} = \frac{E_{cal}}{\Delta t \cdot U_{acc}} \tag{23}$$

  This procedure is repeated for the data of each camera, so that an average current can be calculated on the common tiles (i.e. tile $\#2, \#3, \#6, \#7$). The final vector I_{cal}, which contains the current values on each tile, is reported in Tab. 7 for the pulse #6043. It is worth noticing that for the tiles which are seen by both cameras, the calorimetric estimates of current from *cam 1* are quite similar to those from *cam 2*.

	Tile 1	Tile 2	Tile 3	Tile 4	Tile 5	Tile 6	Tile 7	Tile 8
E_{cam1} [J]	2747	2596	2438	-	3172	2986	2298	-
I_{cam1} [mA]	10.3	9.8	9.1	-	11.9	11.2	8.6	-
E_{cam2} [J]	-	2456	2630	2110	-	2921	2519	2357
I_{cam2} [mA]	-	9.2	9.9	7.9	-	11.0	9.5	8.9
I_{cal} [mA]	10.3	9.5	9.5	8.1	12.2	11.1	9.1	8.9

Table 7: Energies deposited on tiles and related currents for the pulse #6043

Hence, an estimate of the total ionic current produced by the beam for a pulse is obtained by the doubled sum of the currents flowing on each tile, whose values are contained in the I_{cal} vector. The sum is multiplied for a two factor since only the right panel is mounted, so actually STRIKE, in the first experimentation phase, measures only half of the total current of the impinging beam produced by SPIDER.

- Deflection α:
  In general, inside a negative ion accelerator, there are three main factors which can cause deflection of the ion beamlets:
  1) the deformation of the grids under thermal loads;
  2) the electrostatic repulsion among beamlets;
  3) the suppression magnetic field due to the magnets on the EG;
  Inside the accelerator, the relative position of the grid apertures can influence the direction of the beamlet trajectories. In fact, there are two field curvatures inside the EG: one concave at the upstream side (in the PG-EG gap) and one convex at the downstream side (in the EG-GG gap) [27]. The second electric field is stronger, so if, for example, the EG aperture is shifted leftward, the average deflection given by the second curvature prevails and the beamlet is deflected leftward even more. Similarly, since only a concave curvature exists inside the GG because there is no field downstream this grid, if, for example, the GG aperture is offset leftward, the beamlet shows a residual deflection rightward. Hence, if deflections occur, they can be compensated for by proper offsets applied to the apertures [4].
  In order to provide an effective compensation of the deflection caused by the beamlet repulsion and thermal deformations of the grids, a mechanical offset of the grid apertures can be introduced. In particular, the repulsion among ion beamlets causes a transverse outward deflection, which is maximum for the beamlets located at the peripheral apertures, with a consequent increase of the beam divergence both in horizontal and vertical direction. Therefore a compensation by electric field adjustment can be used, which means that proper mechanical offsets are applied at the GG apertures of the involved beamlets.
  For what concerns the deflection due to the electron suppression magnets on the EG, as the polarities of these magnets are alternated from row to row, the beamlet deflection is alternated too, so that a vertical ripple effect occurs [27]. Hence, in order to compensate for this deflection, proper compensation magnets and ferromagnetic material can be added in the GG, instead of using further mechanical offsets on the grid apertures.
  Referring to Fig. 14(b), in the final SPIDER design, deflection has been compensated in different ways depending on the considered segment. Mechanical offsets were applied to all the apertures to compensate for deflection due to thermal deformations. Moreover, for segment $\#1, \#3, \#4$ compensating magnets have been added in the GG, whereas at the bottom of segment #2 further mechanical offsets on the GG apertures were used to compensate for both the repulsion among beamlets and the deflection due to magnets in the EG. Finally, at the top of segment #2 no compensation system was applied, in order to have a reference value for the deflection due to magnets in the EG. Unfortunately, during the installation phase, the compensation magnets for segment $\#1, \#3, \#4$ were arranged with reversed orientation with respect to the nominal one. As a consequence, the overall effect is an increase of the horizontal average deflection on these segments.
  Furthermore, in order to avoid the beamlet overlap on the STRIKE calorimeter and to increase its diagnostic capabilities, a molybdenum mask has been mounted downstream the PG. In particular, the whole beam is subdivided into 4×4 groups of 5×16 beamlets each, as said previously in Sec. 3.1. The tiles are dimensioned to accommodate a single beamlet group but the PG mask selects only five beamlets on each tile. Specifically, by numbering the beamlets in ascending order from top to bottom, the mask selects:
  - in Segment #1 the central beamlets in the vertical positions: $\#2, \#5, \#9, \#12, \#15$;
  - in the other Segments the central beamlets in the vertical positions: $\#2, \#5, \#8, \#12, \#15$;
  This is shown in the following figure, where the selected beamlets are highlighted in red:

[4] Investigations on this aspect for SPIDER have been carried out using a single aperture model and two multi aperture models, developed with the OPERA-3D code [27]

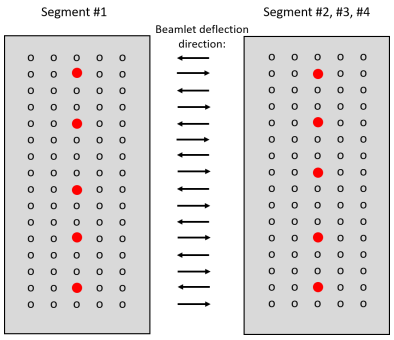

Figure 32: Illustration of Segment #1 (on the left) and of the other segments (on the right) with beamlet groups. Beamlets selected by the molybdenum mask are highlighted in red. Black arrows represent the horizontal direction of beamlet deflection seen on STRIKE tiles at low values of U_{ex}.

Hence, for what concerns the computation of the beamlet deflection along the horizontal axis, in all cases it is defined as:

$$\alpha = \frac{\Delta x}{d} \tag{24}$$

where d is the distance between STRIKE and the GG (fixed at 500 mm in the first experimental phase), and Δx is half of the average horizontal distance between the centre of the five peaks on each tile.
Since deflection is alternated, in Segments #1, #3, #4 (corresponding to tiles #1, #3, #4, #5, #7, #8), by numbering the five peaks of each tile in ascending order from top to bottom (as shown in Fig. 33), the Δx_{mag} is calculated as:

$$\Delta x_{mag} = \frac{\frac{x_{c1}+x_{c4}}{2} - \frac{x_{c2}+x_{c3}+x_{c5}}{3}}{2} \text{ on Segment \#1} \tag{25}$$

$$\Delta x_{mag} = \frac{\frac{x_{c1}+x_{c3}+x_{c4}}{3} - \frac{x_{c2}+x_{c5}}{2}}{2} \text{ on Segment \#3 and \#4} \tag{26}$$

For what concerns Segment #2 (corresponding to tiles #2 and #6), at the top of the tiles (corresponding to the first three peaks) there is no compensation, whereas for the last two peaks another kind of compensation is used, as said previously. So the average distances, called Δx_{no} and Δx_{el}, can be calculated as:

$$\Delta x_{no} = \frac{\frac{x_{c1}+x_{c3}}{2} - x_{c2}}{2} \tag{27}$$

$$\Delta x_{el} = \frac{x_{c4} - x_{c5}}{2} \tag{28}$$

In the following figure, the internal tiles (#1, #2, #3, #4) with numbered peaks are shown at t=5.2 s after the beam start.

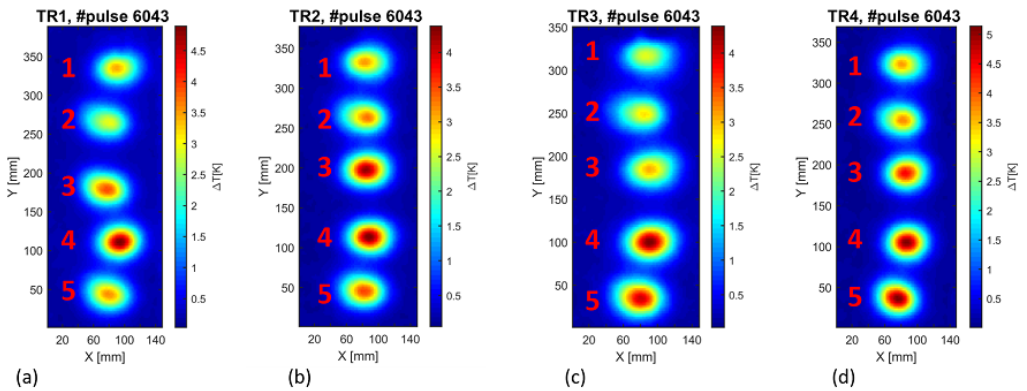

Figure 33: Illustration of tiles #1, #2, #3, #4 with numbered peaks, of pulse #6043, seen by IR cameras at t=5.2 s after the onset of the beam.

- Beam divergence *div*:
  Divergence *div* is correlated to the Gaussian width through the following relation:

$$w_c = w_0 + div \cdot d \tag{29}$$

  where w_c is the Gaussian width calculated from the fit, w_0 is fixed to 4 mm (calculated from previous simulation codes) and d is the distance between STRIKE and the GG (d=500 mm). The horizontal and vertical divergence can be calculated by inverting the Eq. (29).
  Since results appeared not to depend very much on the used frame, it was chosen to analyze the 10th frame of the beam-on phase for each tile. Furthermore, the images given by IR cameras at the 10th frame, were pretty clear and accurate for all the analyzed pulses.

The software and the concepts introduced in this Chapter have been applied to all the data collected by STRIKE. The results of such thorough analysis are reported in the following Chapter.

5 Data Analysis

In this section, the main beam properties are investigated by means of the STRIKE calorimeter. During the first phase of experimental activity, as previously said, only the STRIKE right panel was mounted and it was biased at 60 V. Furthermore cesium was not used, consequently negative hydrogen ions were produced mainly by volume processes. Hence the ratio between co-extracted electrons and negative ions was high.
In order to study the beam optics, many extraction voltage scans have been carried out. Moreover, in order to study other beam dependencies, also vessel pressure scan and filter current scan were executed. Each scan (i.e. each group of shots aiming at studying the beam performance by varying only one parameter at a time) is constituted by shots with two pulses at different values of the varying parameter for a duration of 5 s each.
The experimental data presented in this chapter have been collected in different days, but in the same experimental conditions (i.e. RF Power P_{RF} = 80 kW/gen, the distance between STRIKE and the GG is d=500 mm). Since there are many factors to consider in the estimation of experimental error (such as the spatial resolution of IR cameras, the positioning of STRIKE etc.), the absolute error associated to the calorimeter measurement is difficult to calculate but it is reasonable to assume an uncertainty of about 10%.

5.1 Calorimetry

As described in the previous chapter, by starting from the measured temperature increase ΔT on tiles during the beam-on phase, it is possible to obtain a first estimate of the calorimetric current I_{cal} (see Sec.4.2) carried by negative ions. In order to study how the extracted current varies in different conditions, many scans were executed:

- Extraction potential U_{ex} scan:
  for two different values of the filter current flowing in the PG, I_{filter} = 1.5 kA and I_{filter}= 3 kA, three extraction voltage U_{ex} scans were executed varying the acceleration voltage U_{acc} from 20 kV up to 30 kV. In these scans, the extraction voltage varies in the range of [0.75;3.5] kV, the RF power is P=80 kW/gen, the pulse duration is usually of about 5 s and the acquisition frequency is 5 frames/s. The main current measurement results of the U_{ex} scans are summarized in Tab. 8, 9 and 10. In the following figures, the measured calorimetric current is shown as a function of the extraction voltage:

(a)

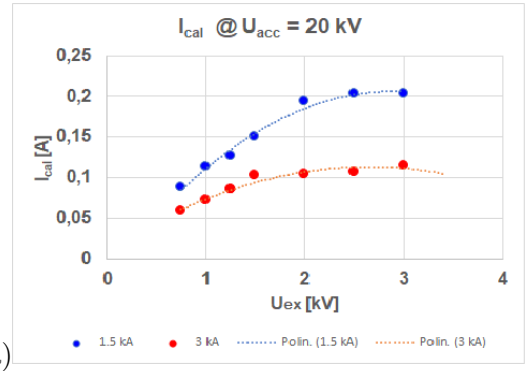

(b)

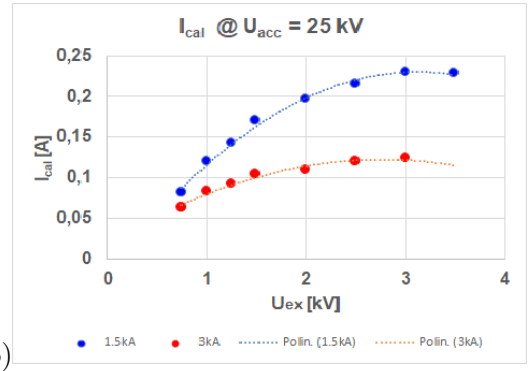

(c)

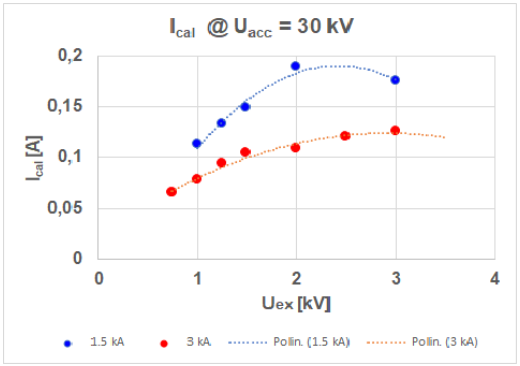

Figure 34: (a) Calorimetric current at U_{acc}= 20 kV (pulse #6225 – #6232 and #6264 – #6272) for I_{filter}=1.5 kA (blue) and I_{filter}=3 kA (red); (b) Calorimetric current at U_{acc}= 25 kV (pulse #6246 – #6250 and #6251 – #6254) for I_{filter}=1.5 kA (blue) and I_{filter}=3 kA (red); (c) Calorimetric current at U_{acc}= 30 kV (pulse #6233 – #6243 and #6256 – #6259) for I_{filter}=1.5 kA (blue) and I_{filter}=3 kA (red).

From these graphs, it is clear that by increasing the extraction potential, the calorimetric current increases until it saturates. When a larger extraction voltage is applied in fact, the extraction electric field can penetrate deeper in the ion source and more negative ions can be extracted. The saturation of the current suggests that, with such plasma density, no more ions are available for extraction. Moreover, as expected, it can be observed that by increasing the filter current, the extracted ion current decreases. In fact, the magnetic filter field generated by I_{filter}, reduces not only the amount of co-extracted electrons, but it also affects negative ions, and consequently the extracted current. In Fig. 34 (b) this behaviour is particularly evident.

(a)

Pulse #	U_{ex} [kV]	I_{cal} [mA]	I_{EG} [A]
6229	1.00	113	9.5
	1.50	150	10.2
6225	2.00	140	10.9
	2.50	203	12.0
6231	2.00	194	11.0
	3.00	204	13.0
6232	0.75	88	9.2
	1.25	127	9.9

(b)

Pulse #	U_{ex} [kV]	I_{cal} [mA]	I_{EG} [A]
6264	0.75	59	5.3
	3.00	115	8.8
6266	1.00	73	5.7
	2.50	107	8.1
6267	1.25	85	6.1
6268	1.25	86	6.2
6272	1.50	102	6.6
	2.00	104	7.3

Table 8: U_{ex} scans at U_{acc} = 20 kV and I_{filter}= 1.5 kA (a), I_{filter} = 3 kA (b).

(a)

Pulse #	U_{ex} [kV]	I_{cal} [mA]	I_{EG} [A]
6246	0.75	81	8.9
	3.00	230	12.3
6247	1.00	120	9.1
	2.50	215	11.4
6248	1.50	170	9.8
	2.00	196	10.7
6250	1.25	142	9.7
	3.50	228	13.6

(b)

Pulse #	U_{ex} [kV]	I_{cal} [mA]	I_{EG} [A]
6251	1.00	83.	5.5
	2.50	120	7.7
6252	1.50	104	6.2
	2.00	109	7.0
6253	0.75	63	5.2
	3.00	124	8.5
6254	1.25	93	5.9
	3.50	108	8.9

Table 9: U_{ex} scans at U_{acc} = 25 kV and I_{filter}= 1.5 kA (a), I_{filter} = 3 kA (b).

(a)

Pulse #	U_{ex} [kV]	I_{cal} [mA]	I_{EG} [A]
6233	1.00	113	9.7
	1.50	149	10.3
6234	2.00	189	11.2
	2.50	135	12.2
6236	1.25	133	9.9
	3.00	130	12.9
6243	2.00	208	10.5

(b)

Pulse #	U_{ex} [kV]	I_{cal} [mA]	I_{EG} [A]
6256	1.25	94	5.9
6257	1.00	78	5.6
	2.50	121	7.7
6258	1.50	104	6.2
	2.00	108	6.9
6259	0.75	65	5.2
	3.00	126	8.4

Table 10: U_{ex} scans at U_{acc} = 30 kV and I_{filter}= 1.5 kA (a), I_{filter} = 3 kA (b).

The graphs show that the maximum extracted current is about 230 mA for U_{ex}=3.5 kV, U_{acc}=25 kV and I_{filter}=1.5 kA (Fig. 34(b)) and the minimum is about 60 mA for U_{ex}=0.75 kV, U_{acc}=20 kV and I_{filter} = 3 kA.
Hence, it is possible to compare these results with other current measurements, such as the current measured at the extraction grid, I_{EG}, and the current measured by the AGPS system, I_{AGPS}. The former is mainly constituted by co-extracted electrons which hit the EG because of the suppression magnets which deviate their trajectory, the latter is constituted by secondary electrons and negative ions. In the first phase of experimentation, the I_{EG} appears to be much larger than the other current measurements (of the order of a few Ampere), which means that much more electrons than negative ions were extracted, as expected since no cesium was used. In Fig. 35 the three current measurements are shown as functions of the filter current I_{filter}. They show a similar pattern: by increasing the filter current, the extracted current decreases, as expected. In particular the I_{EG} decreases by about 56.6%, the I_{AGPS} by about 50.7% and the I_{cal} by about 62.2%. Nevertheless, by comparing the AGPS current and the STRIKE current, they are considerably different: $I_{cal} \approx 35\%\ I_{AGPS}$ (see Fig. 36 (b)).
It was expected to find a calorimetric current smaller than the one measured by AGPS, since STRIKE only measures the equivalent current carried by H^- and H^0 generated by stripping whereas AGPS also measures the secondary electrons[5] but such a remarkable difference between them was not expected. One hypothesis is that most of the accelerated charged particles (i.e. particles registered by AGPS) are produced by the interaction of the beam with the background gas. This explains why they are measured by AGPS but not by the calorimetry, which only measures particles capable to depositing power on the STRIKE tiles.

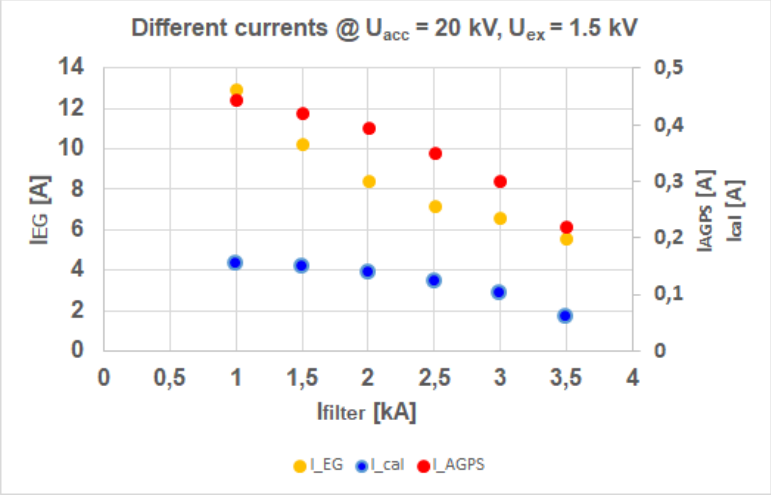

Figure 35: Comparison between different current measurements at U_{acc}= 20 kV and U_{ex}=1.5 kV: calorimetric current I_{cal} (blue), electron current I_{EG} (yellow), AGPS current I_{AGPS} (red) (pulses #6272, #6274, #6275)

[5]The emission of secondary electrons is induced by impact of ions and neutrals on STRIKE surfaces.

The main measurements of the I_{filter} scan are reported in Tab. 11:

Pulse #	I_{filter} [kA]	I_{cal} [mA]	I_{EG} [A]	I_{AGPS} [mA]	div_x [mrad]	div_y [mrad]
6274	2.5	125	7.2	350	41.4	30.9
	2.0	138	8.5	395	37.8	28.4
6275	1.0	156	12.9	446	33.3	27.6
	3.5	59	5.6	220	61.6	37.9
6272	3.0	102	6.6	300	44.6	32.5
6229	1.5	150	10.2	422	34.2	27.4

Table 11: I_{filter} scan at U_{ex} = 1.5 kV and U_{acc}= 20 kV.

Considering the ratio between the electronic current I_{EG} and the ionic current at increasing I_{filter}, as shown in Fig. 36 (a), it is possible to observe that it reaches its minimum at I_{filter} = 2.5 kA for both the ratios $\frac{I_{cal}}{I_{EG}}$ and $\frac{I_{AGPS}}{I_{EG}}$. Furthermore the ratio between the calorimetric current and the AGPS current remains approximately constant at the value of 0.35 at increasing I_{filter}, as shown in Fig. 36 (b).

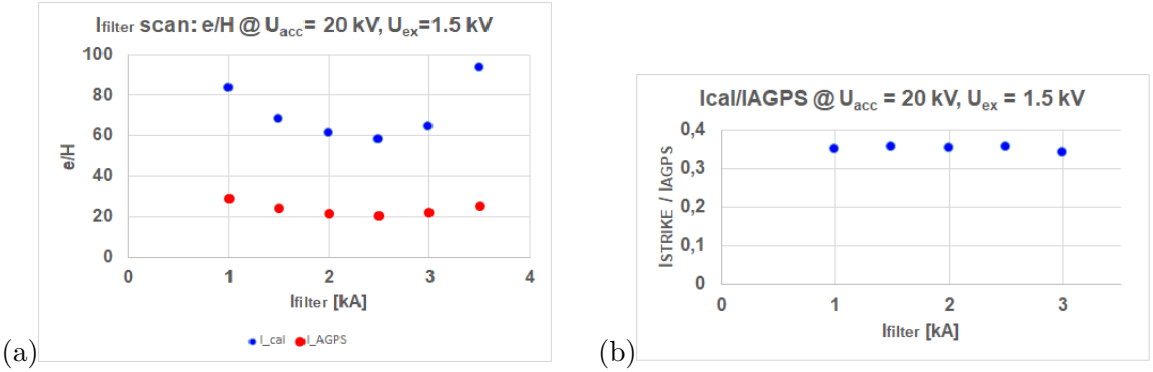

(a) (b)

Figure 36: (a) Ratio between electronic current I_{EG} and the ionic current, given by the calorimetric current I_{cal} (blue) or the AGPS current (red) as a function of the filter current at U_{ex} = 1.5 kV and U_{acc}= 20 kV; (b) Ratio between the calorimetric current and the AGPS current of the I_{filter} scan as a function of I_{filter} at U_{ex} = 1.5 kV and U_{acc}= 20 kV.

- Vessel pressure scan:
  for the pulses #6288 – #6291, by varying the vessel pressure in the range of [24;35] mPa, a pressure scan was executed at two different values of the extraction and acceleration potential:
  - U_{ex} = 1.2 kV and U_{acc} = 20 kV
  - U_{ex} = 2.0 kV and U_{acc} = 30 kV

  The I_{filter} was set at 1.5 kA in both cases. In Tab. 12 the main measurements of the pressure scan are summarized.
  In Fig. 37 (a) the calorimetric current is plotted as a function of the vessel pressure. It can be observed that, as expected, by increasing the vessel pressure, the extracted ion current increases until it seems to saturate. In particular the ion current increases but the electronic current decreases so that the ratio between co-extracted electrons and negative hydrogen ions rapidly decreases, as expected. This is shown in Fig. 37 (b), where the ratio between co-extracted electrons and negative ions clearly decreases as the vessel pressure increases. Such dependence of the source performance on the source pressure is remarkable and is worth to be studied in the test facility SPIDER, particularly in these first campaigns. Nonetheless, towards the ITER requirements, it will be important to improve the performance in the low pressure regime. In particular in the P_{vessel} scan at U_{ex}=1.2 kV, U_{acc}=20 kV, I_{EG} decreases by about 23.2%, whereas I_{cal} increases by about 68.4 %. In the other P_{vessel} scan, at U_{ex}=2 kV and U_{acc}=30 kV, I_{EG} decreases by about 22.9% and I_{cal} increases by 107.5%.

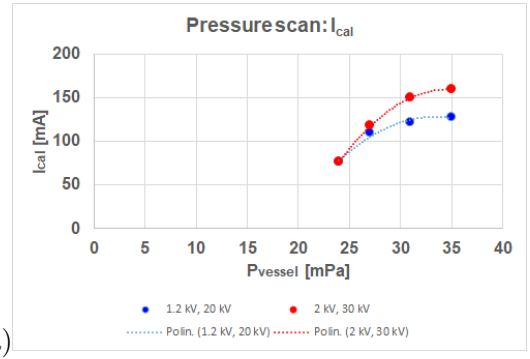

(a)

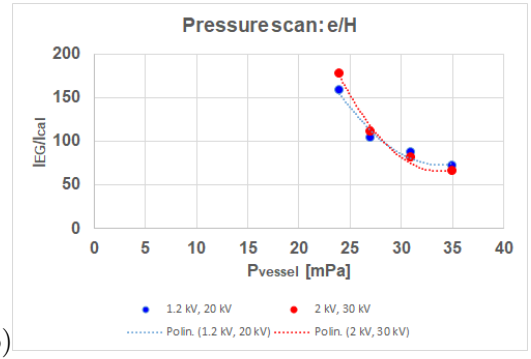

(b)

Figure 37: (a) Calorimetric current at U_{ex}=1.2 kV, U_{acc}= 20 kV (blue) and at U_{ex}=2.0 kV, U_{acc}=30 kV (red); (b) Ratio between electronic and ionic current at U_{ex}=1.2 kV, U_{acc}= 20 kV (blue) and at U_{ex}=2.0 kV, U_{acc}=30 kV (red) as a function of the vessel pressure.

Pulse #	U_{ex} [kV]	U_{acc} [kV]	I_{cal} [mA]	I_{EG} [A]	e^- / H^-	P_{vessel} [mPa]
6288	1.20	20	76	11.9	158	24
	2.00	30	77	13.6	177	24
6289	1.20	20	109	11.3	103	27
	2.00	30	117	12.9	110	27
6290	1.20	20	121	10.6	87	31
	2.00	30	149	12.0	80	31
6291	1.20	20	128	9.2	72	35
	2.00	30	159	10.5	66	35

Table 12: P_{vessel} scan at I_{filter}= 1.5 kA.

- Beam uniformity:
  it was noticed that the calorimetric current flowing on each tile seemed to be slightly different from one to another (of the order of a few mA). In particular, beamlets at the top seemed to carry more current than beamlets at the bottom. Therefore, in order to study the presence of an effective inhomogeneity of the beam, the following parameter was used:

$$\gamma = 100 \cdot \frac{\sigma}{\overline{I_{tile}}} \tag{30}$$

where σ is the standard deviation and $\overline{I_{tile}}$ is the mean of the currents flowing on each tile. In Fig. 38, γ is plotted as a function of the extraction voltage U_{ex} for the pulses of the U_{ex} scan in order to see how the current flowing on each tile effectively varies at increasing extraction voltage. In Fig. 39(a) γ is reported as a function of the filter current for the pulses of the I_{filter} scan, and finally in Fig. 39(b) γ is plotted as a function of the vessel pressure for pulses of the pressure scan.

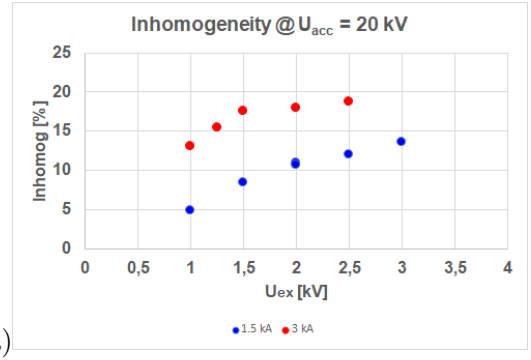

(a)

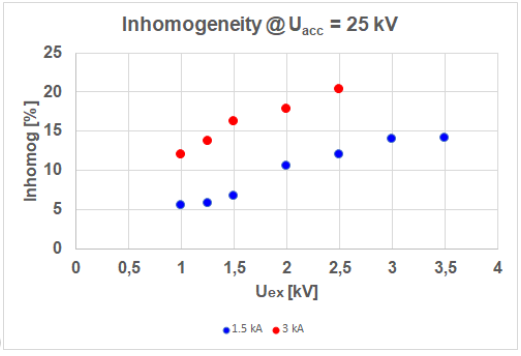

(b)

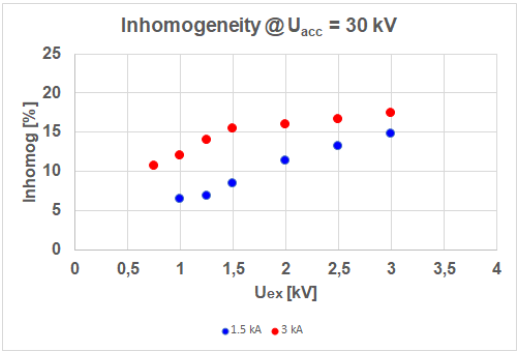

(c)

Figure 38: (a) Inhomogeneity at U_{acc}= 20 kV and I_{filter}=1.5 kA (blue) or I_{filter}=3 kA (red);(b) Inhomogeneity at U_{acc}= 25 kV and I_{filter}=1.5 kA (blue) or I_{filter}=3 kA (red); (c) Inhomogeneity at U_{acc}= 30 kV and I_{filter}=1.5 kA (blue) or I_{filter}=3 kA (red) .

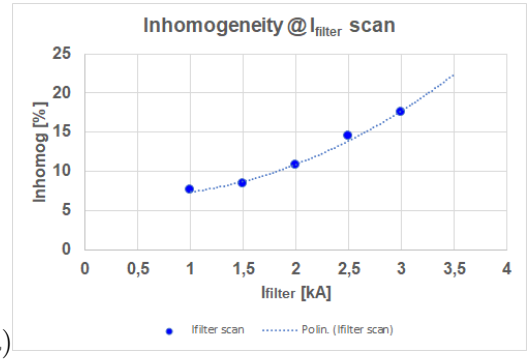

(a)

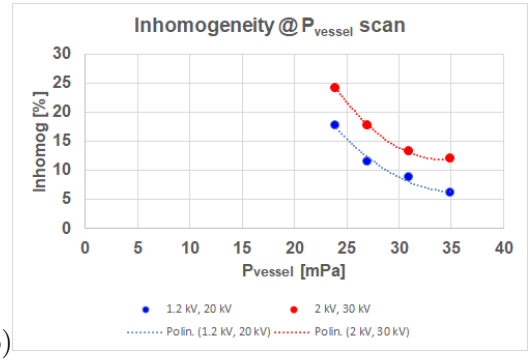

(b)

Figure 39: (a) Inhomogeneity of the I_{filter} scan at U_{ex}= 1.5 kV and U_{acc}=20 kV;(b) Inhomogeneity of the P_{vessel} scan at U_{ex}=1.2 kV, U_{acc}= 20 kV (blue) and at U_{ex}=2 kV, U_{acc}=30 kV (red).

From the figures above, many considerations can be drawn:
- firstly, by increasing the extraction voltage, the beam inhomogeneity also increases;
- secondly, by increasing the filter current, inhomogeneity increases;
- and finally, inhomogeneity decreases as the vessel pressure increases;

It is expected that beam non-uniformity depends on the filter current which creates a horizontal magnetic field which, combined with the electric field due to the different potential between the plasma and surfaces it faces, generates an $\vec{E} \times \vec{B}$ drift in the plasma. Hence, if plasma drifts, it is not homogeneous and consequently also the beam, constituted by H^- from plasma, presents a non-homogeneity. In general, whenever a plasma drift occurs, a beam inhomogeneity might be present. Nevertheless there are many other possible explanations both from the physical and the engineering point of view. For example, non-uniformity can depend on generators, whose power may be slightly different between segments. For what concerns the P_{vessel} scan, it is expected that by increasing pressure, inhomogeneity decreases, since the plasma density increases [6] and consequently the availability of negative ions in the extraction region is larger everywhere and inhomogenities are less visible until U_{ex} is raised. However the phenomenon of inhomogeneity is still under investigation.

Moreover, inhomogeneity can be seen also when evaluating the calorimetric current on different segments normalized to the maximum value between the segments (usually the I_{cal} flowing on segment #1). For example, in Fig, 40 the normalized calorimetric current on segments is shown for the U_{ex} scans at U_{acc} =20 kV and U_{acc}=30 kV with I_{filter} =1.5 kA. It can be easily observed that there is deposited more power, i.e. more current, at the top tiles, and the difference with tiles

[6] *Perfect gas law*: $P = nk_BT$, where P is the gas pressure, n is the gas density for unit of volume, k_B is the Boltzmann constant and T is the gas temperature.

at the bottom increases as the extraction voltage increases. In particular the current difference between segment #1 and #4 in the second U_{ex} scan increases from about 10.7% at U_{ex}= 1 kV to about 29.7% at U_{ex}= 3 kV, as can be better seen in Fig. 41, where the normalized current for all values of the extraction potential is shown [7].

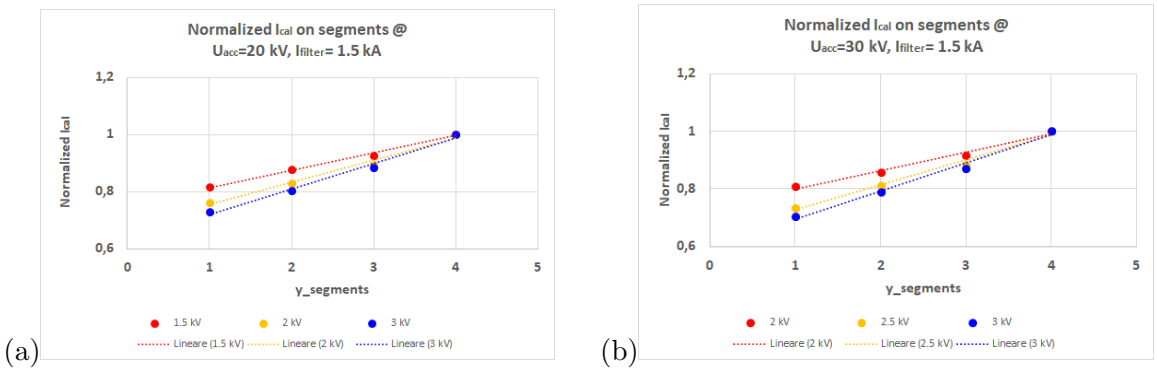

Figure 40: (a) Normalized current on segments at U_{acc}= 20 kV and I_{filter}= 1.5 kA, at three different values of U_{ex}: 1.5 kV (red), 2 kV (yellow), 3 kV (blue) ; (b) Normalized current on segments at U_{acc}= 30 kV, I_{filter}= 1.5 kA, at three different values of U_{ex}: 2 kV (red), 2.5 kV (yellow), 3 kV (blue).

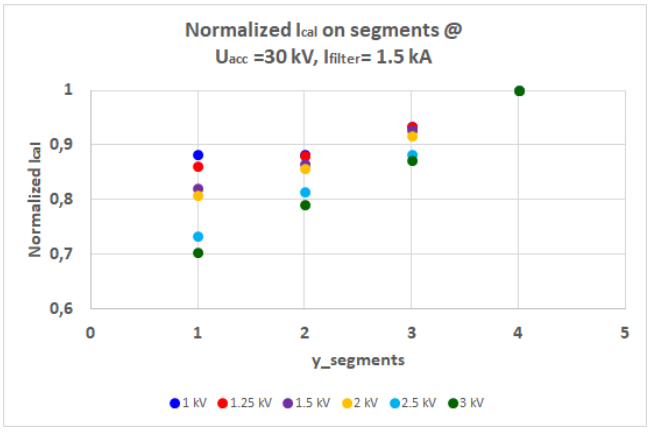

Figure 41: Normalized current on segments at U_{acc}= 30 kV, I_{filter}= 1.5 kA, at different values of U_{ex}: 1 kV (blue), 1.25 kV (red), 1.5 kV (purple), 2 kV (yellow), 2.5 kV (light blue), 3 kV (green).

Similar patterns can be observed for the normalized current of the I_{filter} scan where the difference between current flowing on top and bottom segments increases with increasing of I_{filter}, as shown in Fig. 42 (a)[8]. In particular the current difference between segment #1 and #4 increases from about 15.50% at I_{filter}= 1 kA to about 33.35% at I_{filter}= 3 kA.
On the other hand, for the P_{vessel} scan, it is possible to observe in Fig. 42 (b) that the current difference between segments decreases as the pressure increases, as expected. In particular, the current difference between segment #1 and #4 in the P_{vessel} scan decreases from about 46.95% at P_{vessel}= 24 mPa to about 24.07% at P_{vessel}= 35 mPa.

[7] In Fig. 40 and 41, the vertical axis starts from y=0.6 instead of y=0, in order to better visualize the current patterns.
[8] In Fig. 42(a) the vertical axis starts from y=0.6 instead of y=0, and in Fig. 42(b) the vertical axis starts from y=0.4, in order to better visualize the current patterns.

(a) 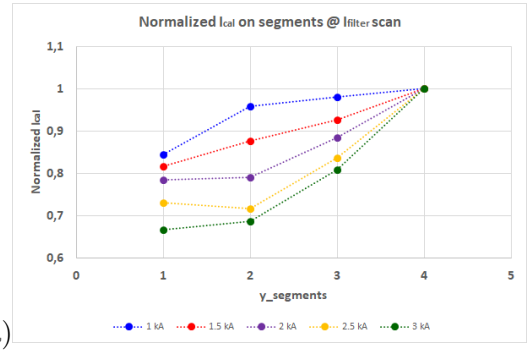

(b) 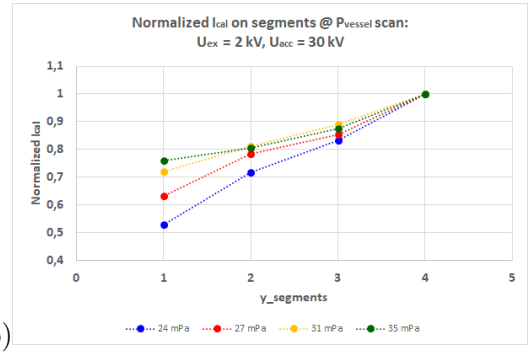

Figure 42: (a) Normalized current on segments at U_{acc}= 20 kV and U_{ex}= 1.5 kV, at different values of I_{filter}: 1 kA (blue), 1.5 kA (red), 2 kA (purple), 2.5 kA (yellow), 3 kA (green); (b) Normalized current on segments at U_{acc}= 30 kV, U_{ex}= 2 kV, at different values of P_{vessel}: 24 mPa (blue), 27 mPa (red), 31 mPa (yellow), 35 mPa (green).

5.2 Divergence

As described at the end of Sec. 4.2, the beamlet shape is reproduced by a 2D Gaussian fit, from which the parameters that are necessary to calculate the beamlet divergence and deflection are obtained. The 1/e beamlet divergence along x axis (horizontal direction) and y axis (vertical direction) were investigated in the extraction potential U_{ex} scans. In these scans, as previously said, the extraction voltage varies in the range of [0.75 ; 3.5] kV, the RF power is P=80 kW/gen and the pulse duration is usually of about 5 s. Moreover, it was chosen to analyze the divergence at the 10th frame of the beam-on phase for each tile, as explained before. Since the acquisition frequency for these pulses is of 5 frames/s, the 10th frame corresponds to t =2 s after the onset of beam.
The main results about horizontal and vertical divergence of the U_{ex} scans are reported in Tab. 13, 14 and 15.

(a)

Pulse #	U_{ex} [kV]	div_x [mrad]	div_y [mrad]
6229	1.00	37.3	32.3
	1.50	34.2	27.4
6225	2.00	34.3	27.9
	2.50	46.1	31.5
6231	2.00	34.8	27.4
	3.00	61.6	33.7
6232	0.75	43.4	37.2
	1.25	37.0	31.2

(b)

Pulse #	U_{ex} [kV]	div_x [mrad]	div_y [mrad]
6264	0.75	51.3	41.1
	3.00	75.3	39.5
6266	1.00	47.9	37.4
	2.50	69.3	38.4
6267	1.25	49.8	36.6
6268	1.25	48.4	36.1
6272	1.50	44.6	32.5
	2.00	55.8	34.0

Table 13: U_{ex} scans at U_{acc} = 20 kV and I_{filter}= 1.5 kA (a), I_{filter} = 3 kA (b).

(a)

Pulse #	U_{ex} [kV]	div_x [mrad]	div_y [mrad]
6246	0.75	56.3	45.9
	3.00	45.9	29.1
6247	1.00	46.3	38.9
	2.50	38.4	26.3
6248	1.50	35.3	28.5
	2.00	35.1	25.4
6250	1.25	38.4	31.5
	3.50	65.0	34.3

(b)

Pulse #	U_{ex} [kV]	div_x [mrad]	div_y [mrad]
6251	1.00	52.9	41.1
	2.50	58.5	33.4
6252	1.50	49.8	36.3
	2.00	54.2	33.9
6253	0.75	59.8	48.1
	3.00	70.1	37.4
6254	1.25	48.2	36.9
	3.50	81.8	41.9

Table 14: U_{ex} scans at U_{acc} = 25 kV and I_{filter}= 1.5 kA (a), I_{filter} = 3 kA (b).

(a)

Pulse #	U_{ex} [kV]	div_x [mrad]	div_y [mrad]
6233	1.00	60.7	47.1
	1.50	45.5	34.1
6234	2.00	38.6	28.3
	2.50	42.7	26.3
6236	1.25	49.4	39.4
	3.00	49.9	28.2
6243	2.00	34.5	27.1

(b)

Pulse #	U_{ex} [kV]	div_x [mrad]	div_y [mrad]
6256	1.25	56.1	42.3
6257	1.00	60.8	46.5
	2.50	57.3	34.1
6258	1.50	49.9	37.9
	2.00	54.2	35.2
6259	0.75	68.7	52.2
	3.00	64.8	35.8

Table 15: U_{ex} scans at U_{acc} = 30 kV and I_{filter}= 1.5 kA (a), I_{filter} = 3 kA (b).

In the following figures, the x (horizontal) and y (vertical) divergence of the pulses of U_{ex} scans at I_{filter} = 1.5 kA are shown as a function of the extraction voltage:

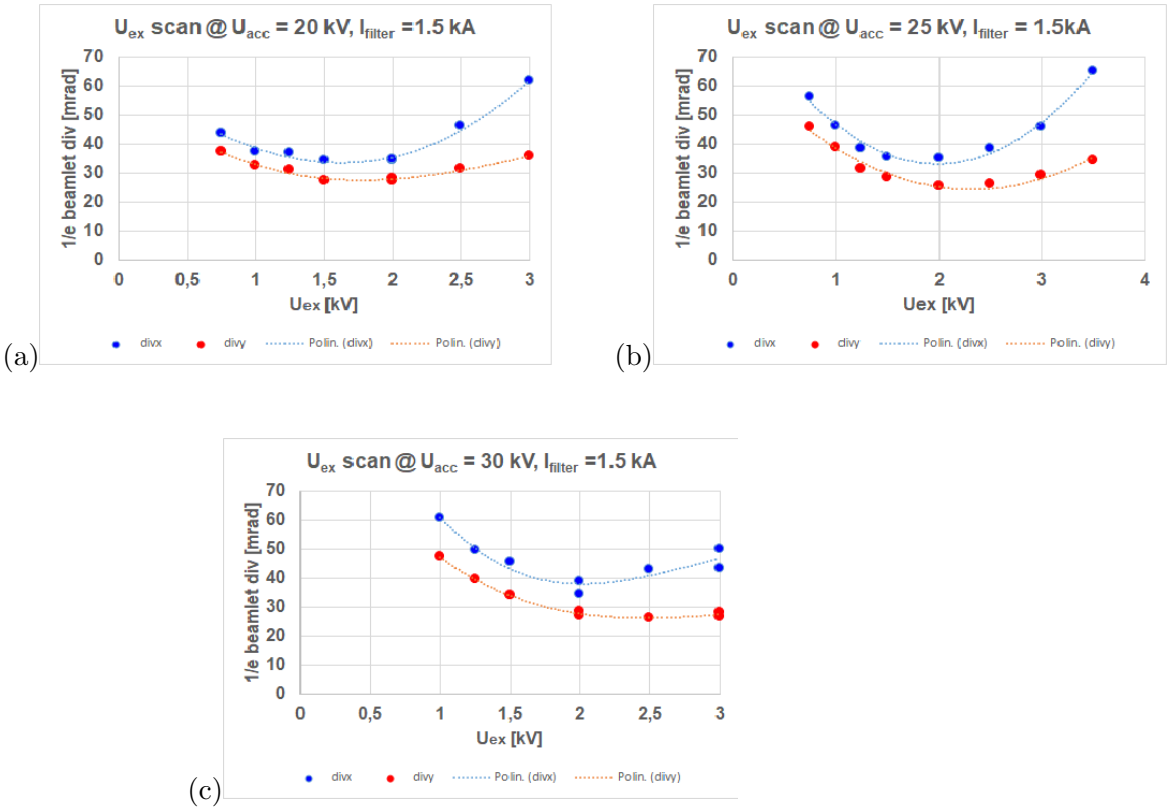

Figure 43: (a) 1/e beamlet divergence at U_{acc}= 20 kV in horizontal direction (blue) and vertical direction (red), pulse #6225 – #6232; (b) 1/e beamlet divergence at U_{acc}= 25 kV in horizontal direction (blue) and vertical direction (red), pulse #6246 – #6250; (c) 1/e beamlet divergence at U_{acc}= 30 kV in horizontal direction (blue) and vertical direction (red), pulse #6233 – #6243, at I_{filter}=1.5 kA.

From the graphs, it can be noticed that the trend, shaped like a "smile", is similar for the divergence along the two axes but the horizontal divergence is always larger than the vertical one. Since the divergence is correlated to the Gaussian width (see Eq. (29)), it means that beamlet shapes are not perfect circumferences but rather approximations of ellipses flattened in the horizontal direction. This is confirmed by looking at the images of the peaks on the STRIKE tiles given by the IR cameras. In the following figure, for example, the images of peak #3 on tile #4 at different U_{ex} of pulse #6250 are reported:

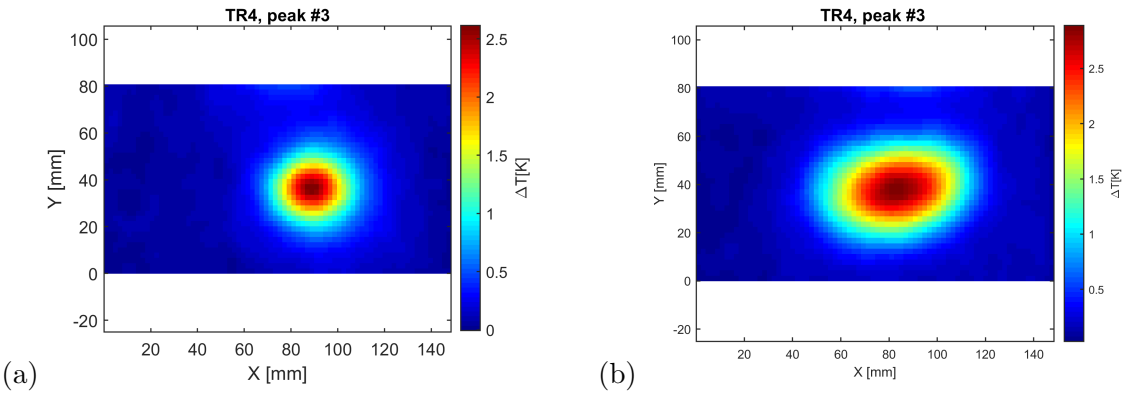

(a) (b)

Figure 44: Image on tile #4 (seen by *cam 2*) of the beamlet divergence of peak #3 at I_{filter}= 1.5 kA, U_{acc}= 25 kV, U_{ex}= 1.25 kV (a) and U_{ex} = 3.5 kV (b), pulse #6250.

As expected, the same behaviour is maintained by the U_{ex} scans at I_{filter} = 3 kA, as shown in Fig. 45. The difference between the horizontal and vertical divergence may be caused by the low extraction and acceleration voltages applied in the first phase of experimentation (less than half the design ones), or by the PG, which is designed to operate at a temperature of 150°C whereas in this experimentation phase it was at only 40°C. In fact, thermal expansion in the accelerator can affect the shape of electrostatic lenses. Many other hypotheses have been proposed, such as a shift of one of the grids, but none of them can be verified before the next SPIDER opening and inspection.

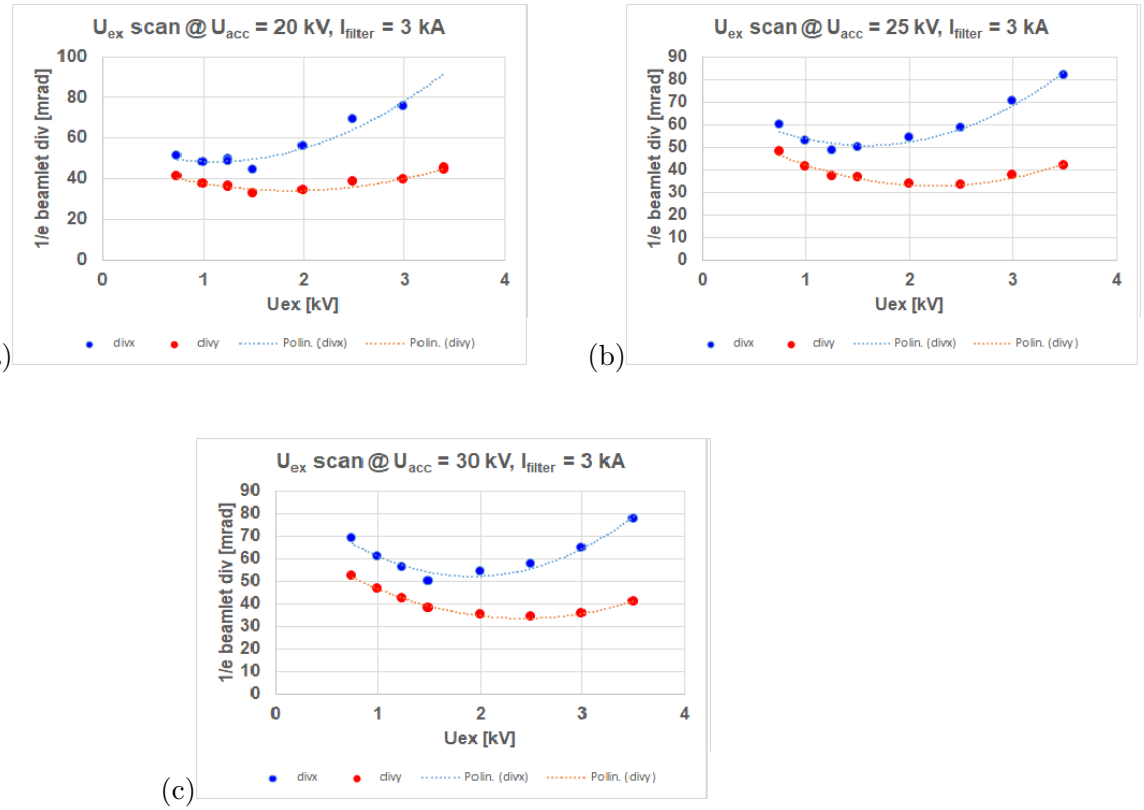

(a) (b) (c)

Figure 45: (a) 1/e beamlet divergence at U_{acc}= 20 kV in horizontal direction (blue) and vertical direction (red), pulse #6264 – #6272; (b) 1/e beamlet divergence at U_{acc}= 25 kV in horizontal direction (blue) and vertical direction (red), pulse #6251 – #6254; (c) 1/e beamlet divergence at U_{acc}= 30 kV in horizontal direction (blue) and vertical direction (red), pulse #6256 – #6259, at I_{filter}= 3 kA.

By comparing the vertical divergence of the U_{ex} scans at different filter current, as shown in Fig. 46(a), it appears that by increasing the I_{filter}, the divergence increases too. In fact, the filter current affects the extracted current, as seen before, consequently also the perveance, which depends linearly on the extracted current itself (see Eq.(16)). In particular, a I_{filter} scan was carried out at U_{acc} = 20 kV and U_{ex} = 1.5 kV (see Tab. 11), and the Fig. 46(b) shows how the horizontal and vertical divergence varies at different filter currents.

(a)

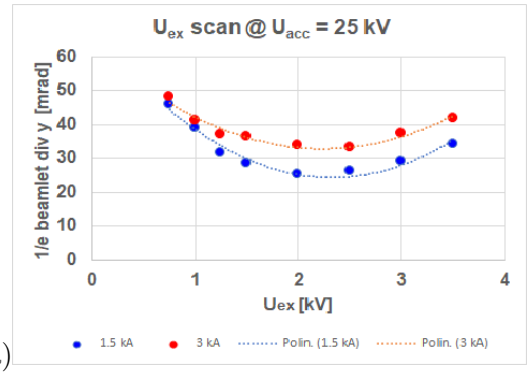

(b)

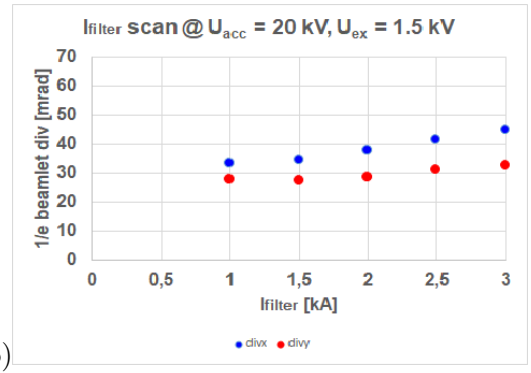

Figure 46: (a) 1/e beamlet vertical divergence as a function of U_{ex} at U_{acc} = 25 kV and I_{filter} = 1.5 kA (blue) and I_{filter}= 3 kA (red); (b) 1/e beamlet divergence in horizontal direction (blue) and vertical direction (red) as a function of I_{filter} at U_{acc} = 20 kV and U_{ex} = 1.5 kV.

From Eq. (19), divergence depends not only on the ratio $\frac{U_{acc}}{U_{ex}}$ but also on the normalized perveance $\frac{P}{P_0}$. Since in the first phase of experimental activity a large amount of co-extracted electrons was part of the beam at the meniscus, it was necessary to take into consideration also the I_{EG} in the computation of experimental perveance P_{exp}:

$$P_{exp} = \frac{I_{ion} + I_{el}\sqrt{\frac{m_e}{m_i}}}{U_{ex}^{\frac{3}{2}} \cdot 80} \tag{31}$$

where I_{ion} is the ionic extracted current (given by the calorimetric current I_{cal}), I_{el} is the electronic current (given by the extraction grid current I_{EG}), m_e and m_i are the electron and the hydrogen ion mass respectively, and U_{ex} is the extraction voltage. It is all divided for 80, which is the number of total beamlets, since perveance is defined on a single beamlet. The maximum perveance, instead, is calculated using Eq. (18), it results equal to $P_{0,exp} = 2.329 \cdot 10^{-7}$ A/V$^{\frac{3}{2}}$.
In the following figures, the horizontal and vertical divergence are shown as functions of normalized perveance for the U_{ex} scans at U_{acc} = 25 kV:

(a)

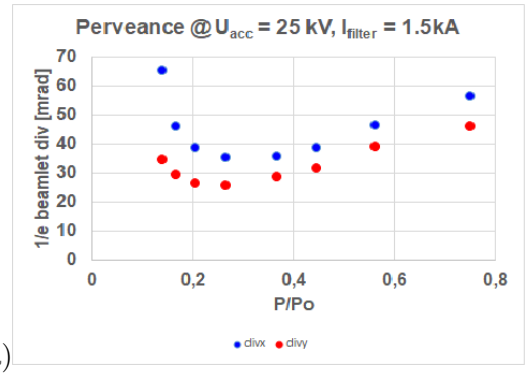

(b)

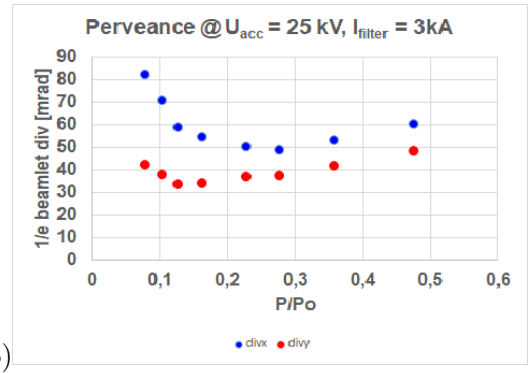

Figure 47: (a) 1/e beamlet divergence at U_{acc}= 25 kV in horizontal direction (blue) and vertical direction (red), pulse #6246 – #6250, at I_{filter}=1.5 kA; (b) 1/e beamlet divergence at U_{acc}= 25 kV in horizontal direction (blue) and vertical direction (red), pulse #6251 – #6254, at I_{filter}=3 kA.

From the graphs above, it is possible to observe that the minimum of beam divergence is different for different I_{filter}. Moreover, comparing the vertical divergence at different acceleration potential, as a function of the ratio $\frac{U_{acc}}{U_{ex}}$, the curves show a similar trend, in particular they seem to reach the minimum of divergence at the same value, as shown in Fig. 48.

(a)

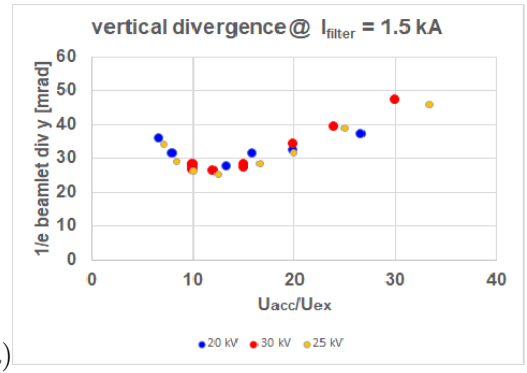

(b)

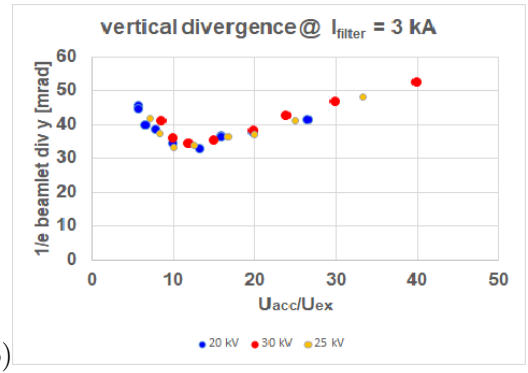

Figure 48: (a) 1/e beamlet vertical divergence at U_{acc}= 20 kV (blue), U_{acc}=25 kV (yellow) and U_{acc}= 30 kV (red), pulse #6229 – #6243 and #6246 – #6250, at I_{filter}=1.5 kA; (b) 1/e beamlet vertical divergence at U_{acc}= 20 kV (blue), U_{acc}=25 kV (yellow) and U_{acc}= 30 kV (red), pulse #6251 – #6259 and #6264 – #6272 at I_{filter}=3 kA.

5.3 Deflection

In general, inside a negative ion accelerator, there are three main factors which can cause deflection of the ion beamlets: the deformation of the grids under thermal loads, the electrostatic repulsion among beamlets, the suppression magnetic field due to the magnets on the EG (see Sec. 4.2). For what concerns the estimation of the beamlet deflection along the horizontal axis, as explained before, if the overall beam is divided into 4 segments, by numbering from up to down (see Fig. 14(b)), in order to compensate for the beamlet deflection, different methods are used depending on the considered segment:
- in Segments #1, #3, #4 permanent magnets are used.
- at the top of Segment #2 deflection is not compensated;
- at the bottom of Segment #2 an electrostatic compensation is adopted;
More details about the compensation system are given in Sec. 4.2.

5.3.1 Horizontal deflection

The different horizontal deflection on segments was calculated as explained at the end of Sec. 4.2 and, as in the case of divergence, it was chosen to analyze the deflection at the 10th frame of the beam-on phase for each tile. Since the acquisition frequency for the analyzed pulses is of 5 frames/s, the 10th frame corresponds to t =2 s after the onset of beam.
In the following Tables, the main results about the different horizontal deflections of the U_{ex} scans are reported. In particular, the average deflection due to magnets in the GG on segments $\#1, \#3, \#4$ is called defl_{mag}; the deflection of the not compensated part of segment #2 is called defl_{no}; and the deflection compensated by electric field at the bottom of segment #2 is called defl_{el}. They are all measured in mrad.

(a)

Pulse #	U_{ex} [kV]	$defl_{mag}$ [mrad]	$defl_{no}$ [mrad]	$defl_{el}$ [mrad]
6229	1.00	24.5	12.9	19.8
	1.50	19.9	9.5	16.2
6225	2.00	18.2	8.7	14.5
	2.50	13.3	5.7	10.4
6231	2.00	17.8	8.1	14.0
	3.00	7.9	2.2	5.5
6232	0.75	26.0	13.9	20.6
	1.25	23.3	12.1	18.9

(b)

Pulse #	U_{ex} [kV]	$defl_{mag}$ [mrad]	$defl_{no}$ [mrad]	$defl_{el}$ [mrad]
6264	0.75	20.9	7.2	15.6
	3.00	3.4	-8.9	-6.4
6266	1.00	18.8	4.9	13.2
	2.50	8.1	-4.6	-0.6
6267	1.25	17.8	4.1	11.9
6268	1.25	17.8	4.0	11.8
6272	1.50	16.4	3.0	10.5
	2.00	12.3	-1.0	4.9

Table 16: U_{ex} scans at U_{acc} = 20 kV and I_{filter}= 1.5 kA (a), I_{filter} = 3 kA (b).

(a)

Pulse #	U_{ex} [kV]	$defl_{mag}$ [mrad]	$defl_{no}$ [mrad]	$defl_{el}$ [mrad]
6246	0.75	23.7	13.1	18.7
	3.00	8.1	1.5	5.7
6247	1.00	21.9	11.5	17.8
	2.50	11.0	2.9	8.4
6248	1.50	18.3	8.3	14.9
	2.00	13.8	4.5	10.8
6250	1.25	19.9	9.5	16.4
	3.50	2.5	-2.5	0.5

(b)

Pulse #	U_{ex} [kV]	$defl_{mag}$ [mrad]	$defl_{no}$ [mrad]	$defl_{el}$ [mrad]
6251	1.00	17.9	5.4	13.1
	2.50	7.8	-3.9	0.3
6252	1.50	14.7	1.9	9.6
	2.00	11.1	-0.9	4.7
6253	0.75	19.6	7.1	15.1
	3.00	4.3	-6.7	-3.6
6254	1.25	16.0	3.3	10.9
	3.50	0.6	-10.1	-8.2

Table 17: U_{ex} scans at U_{acc} = 25 kV and I_{filter}= 1.5 kA (a), I_{filter} = 3 kA (b).

(a)

Pulse #	U_{ex} [kV]	$defl_{mag}$ [mrad]	$defl_{no}$ [mrad]	$defl_{el}$ [mrad]
6233	1.00	19.2	8.7	16.4
	1.50	13.7	3.2	10.9
6234	2.00	11.8	1.7	9.1
	2.50	7.3	-1.5	4.7
6236	1.25	17.5	7.0	14.6
	3.00	4.8	-2.7	2.3
6243	3.00	6.3	-0.7	4.3

Pulse #	U_{ex} [kV]	$defl_{mag}$ [mrad]	$defl_{no}$ [mrad]	$defl_{el}$ [mrad]
6256	1.25	15.2	3.1	11.1
	3.50	0.4	-9.1	-6.8
6257	1.00	16.9	5.1	13.3
	2.50	7.3	-4.0	1.1
6258	1.50	13.3	1.4	8.9
	2.00	10.1	-1.5	4.8
6259	0.75	18.5	6.5	14.6
	3.00	4.4	-6.4	-2.4

(b)

Table 18: U_{ex} scans at U_{acc} = 30 kV and I_{filter}= 1.5 kA (a), I_{filter} = 3 kA (b).

First of all, the magnetic compensation on the three segments (#1, #3, #4) has been investigated. It appears to be slightly different from a segment to another, maybe this is due to the slightly different current carried on the tiles by the impinging beamlets (see the inhomogeneity paragraph). The largest difference between the magnetic deflection on segments is about 15%, and it increases as the extraction potential increases, which is reasonable since beam inhomogeneity increases too with increasing U_{ex}. In the following figure, as an example, the magnetic deflection on segments as a function of the extraction voltage is shown for pulses #6229 – #6232 at U_{acc} = 20 kV and I_{filter} = 1.5 kA.

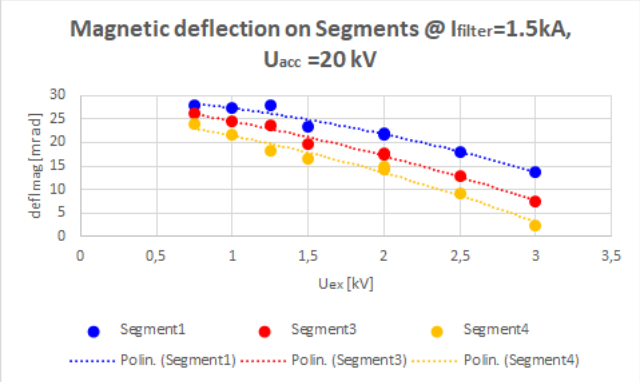

Figure 49: Magnetic deflection on segments #1 (blue), #3 (red) and #4 (yellow) for pulses of the U_{ex} scan at U_{acc} = 20 kV and I_{filter} = 1.5 kA.

By considering the average magnetic deflection, it is possible to compare it at different acceleration voltage U_{acc}, as shown in Fig. 50. The three curves follow a similar downward trend as the extraction voltage increases. Moreover it is possible to notice that by increasing the acceleration potential, magnetic deflection decreases, as expected:

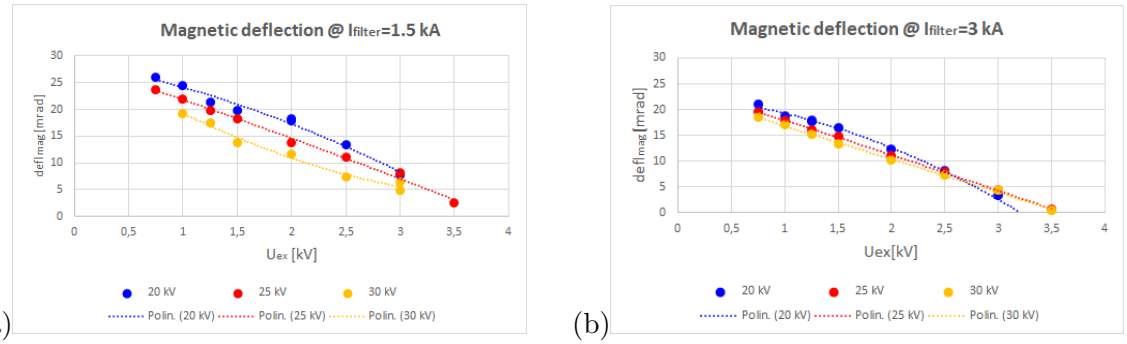

(a) (b)

Figure 50: Average magnetic deflection at different acceleration potential: U_{acc}= 20 kV (blue), U_{acc}= 25 kV (red) and U_{acc}=30 kV (yellow) at I_{filter} = 1.5 kA (a) and I_{filter}= 3 kA (b).

From tests and simulations, it was expected that deflection would be proportional to the inverse square root of the extraction potential:

$$\alpha \propto \frac{1}{\sqrt{U_{ex}}} \tag{32}$$

Nevertheless, data show a completely different trend. It was assumed that in the first phase of experimentation, shots have been done at extraction and acceleration voltage too low compared to those for which SPIDER was designed. However this is still an open issue.
The same decreasing trend is followed by the electrical deflection and by the deflection of the uncompensated part of segment #2, as could be seen in the following figures, where the three horizontal deflections are compared as functions of U_{ex}.

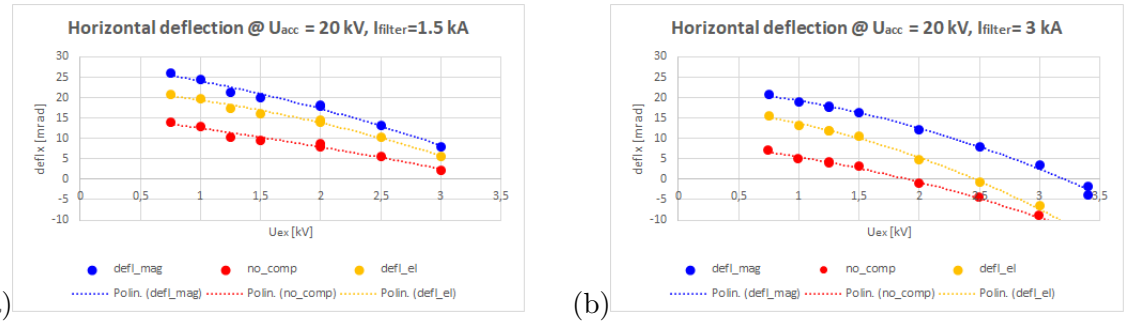

(a) (b)

Figure 51: Comparison between different horizontal deflections: magnetic deflection (blue), electrical deflection (yellow) and uncompensated deflection (red) at U_{acc}= 20 kV and I_{filter} = 1.5 kA (a), I_{filter}= 3 kA (b).

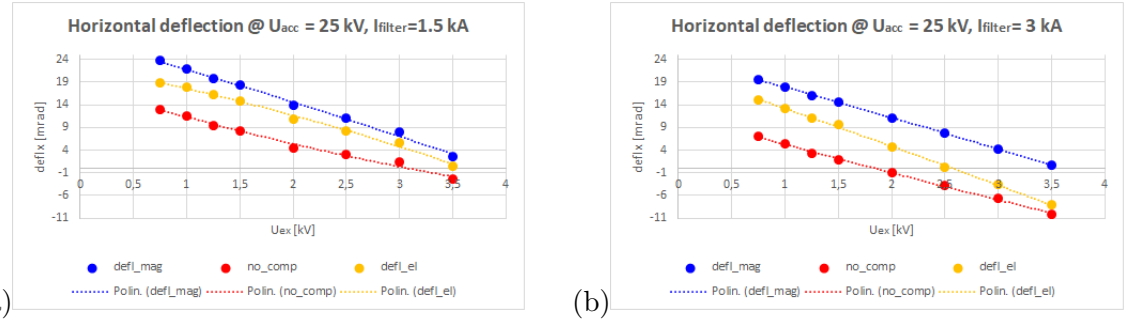

(a) (b)

Figure 52: Comparison between different horizontal deflections: magnetic deflection (blue), electrical deflection (yellow) and uncompensated deflection (red) at U_{acc}= 25 kV and I_{filter} = 1.5 kA (a), I_{filter}= 3 kA (b).

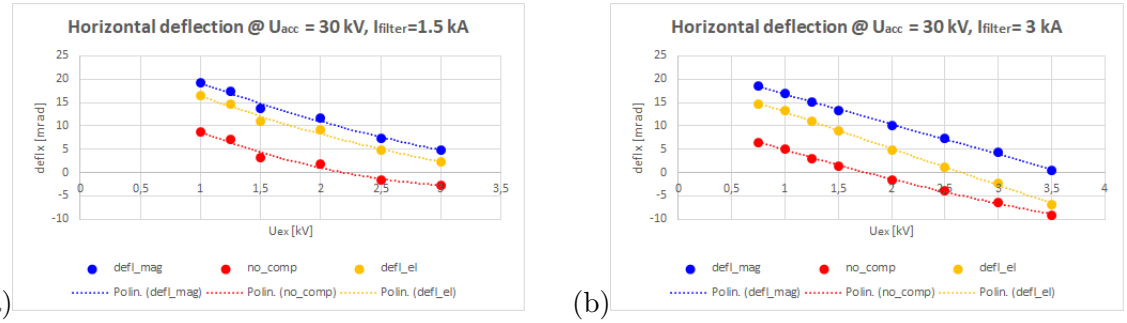

(a) (b)

Figure 53: Comparison between different horizontal deflections: magnetic deflection (blue), electrical deflection (yellow) and uncompensated deflection (red) at U_{acc}= 30 kV and I_{filter} = 1.5 kA (a), I_{filter}= 3 kA (b).

Many considerations can be drawn looking at the graphs above:
- firstly, as expected, the magnetic deflection is always the worst of the three, since the compensating magnets in the GG actually "de-compensate" the overall deflection of beamlets;
- secondly, only for the U_{ex} scan at U_{acc}= 30 kV and I_{filter} = 1.5 kA (Fig. 53(a)) the trend seems similar to that expected from Eq. (32), even if sign changes of deflection were not expected;
- thirdly, the uncompensated part of segment #2 shows a deflection lower than the part electrically compensated, as highlighted in Fig. 55 where tiles #2 and #6 of pulse #6274 are displayed;
- moreover, on segment #2, both the deflections assume negative values for high U_{ex}, although for higher filter current the change of sign occurs at lower extraction voltages;
This strange behaviour can also be observed from the images provided by IR cameras on segment #2. For example, by considering the worst deflections, i.e. pulses at U_{acc}= 25 kV and I_{filter} = 3 kA, where deflections reach very negative values (such as $defl_{no}$= -10.1 mrad and $defl_{el}$= -8.4 mrad at U_{ex} = 3.5 kV), the sequence of the images of impinging beamlets on tile #2 given by *cam 1* at increasing extraction voltage, is shown in Fig. 54.
Even in this case, it is assumed that this strange trend is due to the low voltages used in this experimentation phase, however it remains still an open issue that needs to be further investigated.

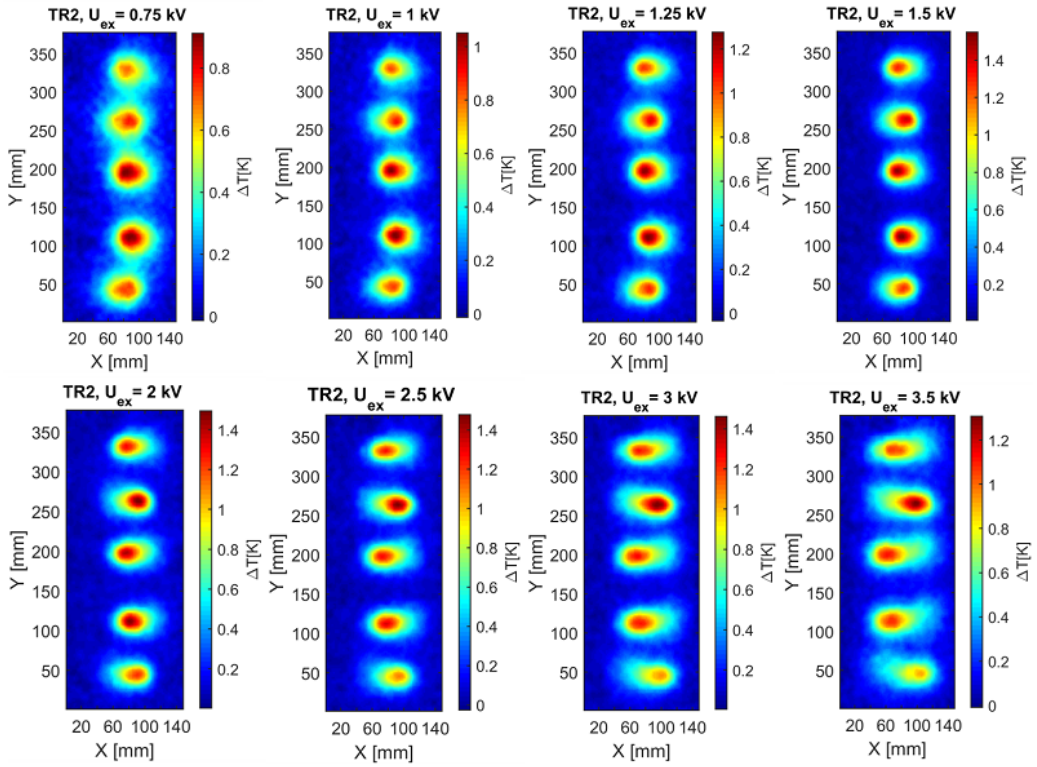

Figure 54: U_{ex} scans at U_{acc}= 25 kV and I_{filter} = 3 kA: images of Tile #2 seen by *cam 1* at t= 2 s after the onset of beam, at increasing extraction voltage U_{ex}, pulses #6251 – #6254.

From the sequence of figures above, it is possible to observe clearly how the beamlet centres move at increasing extraction voltage. Hence, the negative values of deflection are explained since, for high extraction potential, the beamlet centres completely change their position, moving towards the opposite expected direction.
Nevertheless, it still remains an open issue why the uncompensated part of segment #2 has a lower deflection than the one electrically compensated. This could be seen by the sequence above, but it is more highlighted in the following figure where tiles #2 and #6 of pulse #6274 are shown.

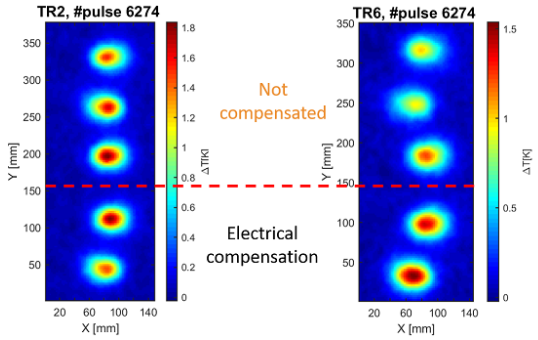

Figure 55: Illustration of the different deflection compensation on segment #2 (i.e. tiles #2 and #6) of pulse #6274 at U_{acc} =20 kV, U_{ex} = 1.5 kV, I_{filter}= 2.5 kA at t=2 s after the onset of the beam.

5.3.2 Vertical deflection

From the I_{filter} scan at U_{ex}= 1.5 kV and U_{acc} = 20 kV, it is possible to observe how the vertical position of the peak centres varies at different filter currents. In fact, the current I_{filter} flowing in the PG, provides a horizontal magnetic field, whose intensity depends on the current intensity. The negatively charged particles, constituting the beamlets, feel this magnetic field and consequently their vertical position varies with varying of magnetic field intensity. In Tab. 19 the positions of the five peak centres (obtained by the 2D Gaussian fit, as explained in Sec. 4.1) on tile #1 of the I_{filter} scan are reported.

Pulse #	I_{filter} [kA]	y_{c1} [mm]	y_{c2} [mm]	y_{c3} [mm]	y_{c4} [mm]	y_{c5} [mm]
6274	2.5	334.7	266.4	179.6	111.8	44.5
	2.0	334.8	266.9	180.1	112.3	44.8
6275	1.0	335.4	267.4	180.6	113.0	45.7
	3.5	332.3	264.4	178.1	110.9	43.3
6272	3.0	334.4	265.9	179.2	111.4	43.8
6229	1.5	335.3	267.3	180.3	112.7	45.2

Table 19: Vertical positions of peak centres on tile #1 in I_{filter} scan at U_{ex} = 1.5 kV and U_{acc}= 20 kV.

In the following figures the vertical position of peak centres at different filter current is shown. In particular, in Fig. 56(b) only the position of the 5th peak is reported in order to better visualize its pattern. As expected, by increasing the I_{filter}, the vertical position of the beamlets decreases.

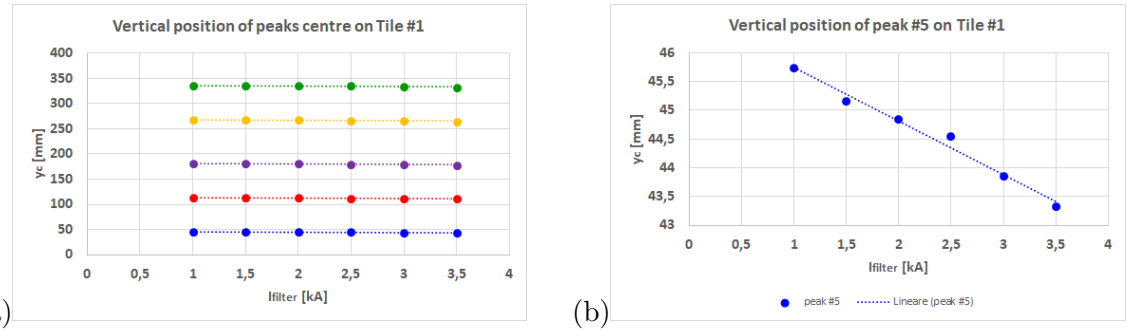

Figure 56: I_{filter} scan at U_{ex}=1.5 kV and U_{acc}= 20 kV: (a) vertical positions of peak centres on tile #1 as a function of I_{filter}: peak #1 (green), #2 (yellow), #3 (purple), #4 (red), #5 (blue); (b) vertical position of the 5th peak centre on tile #1 as a function of I_{filter}.

Moreover, if the vertical position of beamlet centre at I_{filter}=3.5 kA is shifted in y = 0 for all the five peaks (all the other vertical positions are shifted consequently), it is possible to compare the decreasing on the five peaks together, as shown in the following figure. In particular, peak #1 decreases by about 3 mm whereas peak #5 by 2.5 mm.

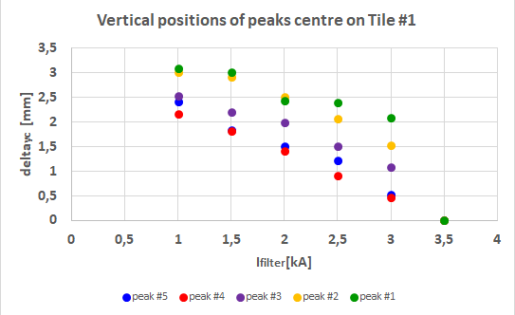

Figure 57: I_{filter} scan at U_{ex}=1.5 kV and U_{acc}= 20 kV: vertical shifted positions of peak centres on tile #1 as a function of I_{filter}: peak #1 (green), #2 (yellow), #3 (purple), #4 (red), #5 (blue) .

6 Conclusions

The ITER tokamak is an international project, whose aim is to prove the possibility to produce energy by nuclear fusion of deuterium and tritium nuclei with a sufficient efficiency and for a reasonable duration of time (up to one hour for ITER). In order to reach the high temperatures necessary for thermonuclear fusion, additional heating systems are required, such as the injection of a neutral beam. The main component of a Neutral Beam Injector (NBI) is a Radio Frequency (RF) source which creates negative hydrogen or deuterium ions. The test facility SPIDER (**S**ource for the **P**roduction of **I**ons of **D**euterium **E**xtracted from an **R**F plasma) was built at Consorzio RFX in Padova (Italy), in order to study and optimize negative ion production for the ITER neutral beam injectors. The ion source SPIDER is provided with many diagnostics, one of which is the high-spatial-resolution calorimeter STRIKE (**S**hort-**T**ime **R**etractable **I**nstrumented **K**alorimeter **E**xperiment). The main aim of STRIKE is the characterization of the SPIDER beam during short operations (several seconds).
The most important measurements performed by STRIKE are: beam uniformity and current, beam divergence and particle losses due to the beam interaction with the background gas. The main components of STRIKE are 16 one-directional (1D) Carbon Fiber Composite (CFC) tiles (of size: 376 $\times$ 142 $\times$ 20 mm^3), exposed perpendicularly to the beam, at varying distance between 0.5 m and 1.1 m downstream the Grounded Grid (GG). The tiles are observed on the rear side by two infrared (IR) thermal cameras in order to determine the spatial distribution of power within the beam, constituted by 4 $\times$ 4 groups of 5 (horizontally) $\times$ 16 (vertically) beamlets each.
During the first phase of experimentation, only the STRIKE right panel (i.e. only 8 tiles) was installed and it was biased at 60 V. Moreover, in order to avoid an overlap of the beamlets on the STRIKE calorimeter and to increase its diagnostic capabilities, a molybdenum mask, selecting only 5 beamlets per tile, was installed in front of the Plasma Grid (PG). Furthermore cesium was not used, consequently negative hydrogen ions were produced mainly by volume processes. Hence the ratio between co-extracted electrons and negative ions was high. The electrons which are extracted together with the negative ions are dumped onto the Extraction Grid (EG) by a magnet system ("suppression magnets") located in the EG itself, so that also the electronic current I_{EG} can be measured.
The error associated to the calorimeter measurements is difficult to be estimated but it is reasonable to assume an uncertainty of about 10%. In order to analyze the IR images, a data analysis software has been developed through the programming language MATLAB.
The main goal of the present thesis was to give a first characterization of the SPIDER negative ion beam by means of the STRIKE calorimeter.

6.1 Main results

In order to investigate the beam properties, several extraction voltage scans were executed at different values of acceleration voltage and filter field current. Moreover two source pressure scans were executed at different extraction and acceleration voltage. Finally a scan of the filter current flowing in the Plasma Grid (PG) was executed.
From the calorimetry, it is found that, as expected, by increasing the extraction voltage, the calorimetric current increases too until it saturates. Moreover, there is less ion current as the filter current increases, which is reasonable since the filter current aims at reducing the co-extracted electrons but it also affects negative ions, and consequently the extracted current itself. Furthermore, as the source pressure increases, the ion current increases and the electron current decreases so that the ratio between co-extracted electrons and negative hydrogen ions rapidly decreases, as expected. The extractable ion current is measured also by the acceleration grid power supply (AGPS), so that it is possible to compare it with the current given by calorimetry. The latter is found to be much lower than the AGPS current, in particular $I_{cal} \approx 35\%\ I_{AGPS}$. One hypothesis is that most of the accelerated charged particles (i.e. particles registered by AGPS) are produced by the interaction of the beam with the background gas. This explains why they are measured by AGPS but not by the calorimetry, which only measures particles capable to depositing power on the STRIKE tiles. However the phenomenon is still under investigation.

For what concerns the beam homogeneity, it is noticed that more power is deposited on tiles at the top than those at the bottom. As expected this non-uniformity increases at increasing extraction voltage. Furthermore it increases as the filter current increases and it decreases with increasing pressure. This behaviour is possibly due to drifts arising in the plasma because of the presence of magnetic and electric fields. There may be other explanations both from the physical and the engineering point of view, however the beam homogeneity needs to be further investigated in the future experimental campaign, being homogeneity one crucial requirement for the ITER neutral beam injector.
Beamlet shape is reproduced in the analysis program by a 2D Gaussian fit, from which the parameters needed to estimate beamlet divergence and deflection are obtained. In particular the 1/e beamlet horizontal and vertical divergence have been studied in the extraction voltage scans. It is found that by increasing extraction voltage, divergence shows a trend shaped like a "smile", as expected. Nevertheless, horizontal and vertical divergence for each scan have different values. Particularly, by looking at the images given by IR cameras, the beamlet shape is similar to an ellipse flattened in the horizontal direction, and not a perfect circumference, as one would expect. Many hypotheses have been proposed, such as a shift of one of the grids, or the low extraction and acceleration voltage applied (less than half the ones for which SPIDER is designed). In the next future, higher voltages will be applied and the beamlet divergence will be further investigated.
In general, inside a negative ion accelerator, there are three main factors which can cause deflection of the ion beamlets: the deformation of the grids under thermal loads due to stray particles from the beam, the electrostatic repulsion among beamlets, the suppression magnetic field due to the magnets in the Extraction Grid (EG). In the first experimentation phase, compensation for beamlet deflection has been done in different ways: in tiles $\#1, \#3, \#4, \#5, \#7, \#8$ permanent magnets, mounted upside down, are used; at the top of tiles $\#2, \#6$ deflection is not compensated whereas at the bottom an electrostatic compensation is adopted. By considering tiles where the magnetic compensation system is used, firstly it is found that deflection decreases as extraction voltage increases, as expected. Moreover, deflection appears to be different between the three segments. It is assumed that this is due to the inhomogeneity of the beam, i.e. the slightly different current flowing on tiles. In addition, at increasing acceleration voltage, magnetic deflection decreases. However, due to errors in the assembly phase, the compensation magnets in the Grounded Grid (GG) actually "de-compensate" the overall deflection of beamlets so that, by comparing the three different compensation methods, the magnetic compensation appears to be the worst. By considering tiles #2 and #6, the uncompensated part shows a lower deflection than the part electrically compensated and for high values of the extraction voltage, deflections assume negative values. This strange trend was not expected since deflection should be proportional to the inverse square root of the extraction potential. Even in this case, many hypotheses have been proposed but further investigations are needed. For the filter current scan, it was observed that the vertical position of the peak centres decreases as the filter current increases, as expected. In fact the negatively charged particles of the beam feel the horizontal magnetic field, whose intensity depends on the filter current itself.
Finally, there are still many open issues that need to be further investigated. More investigations about the SPIDER negative ion beam will be carried out in the very next future. Better estimates of the measured parameters (beam current, divergence, deflection) could be obtained with the use of cesium, with higher values of the extraction and acceleration potentials, with higher values of the filter current and when even the STRIKE left panel will be installed.

References

[1] M. Kikuchi et al., *Fusion Physics*, International Atomic Energy Agency, Vienna (2012)

[2] J.K. Shultis et al., *Fundamentals of nuclear science and engineering*, CRC Press, p. 151, iSBN 0-8247-0834-2 (2002)

[3] W. Kraus, *CERN Accelerator School - Ion Sources* (2012)

[4] A. Kojima et al., *Analysis on acceleration of DT-mixed ion beams in a negative ion accelerator for a DT-mixed Neutral Beam Injector*, Fusion Eng. Des., Vol. 121, p.145-151, (2017)

[5] Mark D. Boyer et al., *Backstepping Control of the Toroidal Plasma Current Profile in the DIII-D Tokamak*, IEEE Transactions on Control Systems Technology, Vol. 22, p. 1725-1739, (2014)

[6] Max-Planck Institut fur Plasmaphysik official website, www.ipp.mpg.de

[7] V. Toigo et al., *The PRIMA Test Facility: SPIDER and MITICA test-beds for ITER neutral beam injectors*, New. J. Phys. **19** 085004, (2017)

[8] R. Pasqualotto et al., *Diagnostic of the ITER neutral beam test facility*, Rev. Sci. Instrum. **83**, 02B103 (2012)

[9] G. Serianni et al. *Thermal simulations of STRIKE tiles for the assessment of the CFC prototypes and of the configuration for SPIDER*, AIP Conf. Proc. **1515**, 579, (2013)

[10] G. Serianni et al., *First negative ion beam measurement by the Short-Time Retractable Instrumented Kalorimeter Experiment*, Rev. Sci. Instrum. **85**, 02A736 (2014);

[11] G. Serianni, *Negative Ion Beam characterisation in BATMAN by mini-STRIKE: Improved Design and New Measurements*, AIP Conf. Proc. **1655**, 060007 (2015)

[12] G. Serianni et al., *Test of 1D carbon-carbon composite prototype tiles for the SPIDER diagnostic calorimeter*, AIP Conf. Proc. **1869**, 060007 (2017)

[13] G. Serianni et al., *Thermal and electrostatic simulations of the diagnostic calorimeter for the Source for Production of Ion of Deuterium Extracted from RF plasma beam*, Rev. Sci. Instrum. **83**, 02B725 (2012)

[14] P. Sonato et al., *The ITER full size plasma source device design*, Fusion Eng. Des., vol. 84, pp. 269-274, (2009)

[15] V. Antoni et al., *Design, Installation, commissioning and operation of a beamlet monitor in the negative ion beam test stand at NIFS*, AIP Conf. Proc. **1655**, 060005 (2015)

[16] ITER official website, www.iter.org

[17] The Controlled Fusion Atomic Data Center official website, www-cfadc.phy.ornl.gov

[18] David Young http://www.robots.ox.ac.uk/%7Evgg/presentations/bmvc97/criminispaper/node3.html, University of Sussex (2008)

[19] A. Pimazzoni et al., *A First Characterization of NIO1 Particle Beam by Means of a Diagnostic Calorimeter*, AIP Conf. Proc. **1869**, 030028 (2017)

[20] A. Rizzolo et al., *Final design of the diagnostic calorimeter for the negative ion source SPIDER*, Fusion Eng. Des., vol. 123 (2017)

[21] M. De Muri et al., *Design and specifications of the diagnostics for the instrumented calorimeter of Source for the Production of Ions of Deuterium Extracted from Radio frequency plasma*, Rev. Sci. Instrum. **83**, 02B724 (2012);

[22] M. Boldrin et al., Fusion Eng. Des. **84**, 466 (2009)

[23] M. Dalla Palma et al., Final Report of EFDA Contract No. F4E-2008-GRT-011-01 (PMS-H.CD) T3.9/D2.2.2, 2009 (not published)

[24] P. Franzen et al., *Performance of multi-aperture grid extraction systems for an ITER relevant RF-driven negative hydrogen ion source*, Nucl. Fusion **51**, 073035 (2011)

[25] R. Gutser et al., *Negative hydrogen ion transport in RF-driven ion sources for ITER NBI*, Plasma Phys. Control. Fusion **51**, 045005 (2009)

[26] I. G. Brown, *The Physics and Technology of Ion Sources*, Wiley-VCH Verlag GrnbH & Co. KGaA, Weinheim (2004)

[27] P. Agostinetti et al., *Physics and engineering design of the Accelerator and Electron Dump for SPIDER*, Nucl. Fusion **51**, 063004 (16pp) (2011)

Ringraziamenti

Desidero ringraziare tutti coloro che mi hanno aiutato e sostenuto in questi tre splendidi anni di Università, nei quali credo di essere maturata sia nella mia grande passione che è la Fisica, ma anche e soprattutto come persona.
In primo luogo vorrei ringraziare il mio relatore, Dr. Gianluigi Serianni, e il mio correlatore, Dr. Antonio Pimazzoni, per i loro preziosi consigli e la loro guida sapiente nella stesura della tesi.
Proseguo nel ringraziare la Prof.ssa Roberta Bolzanello, docente di Fisica presso il liceo Scientifico Democrito di Roma, alla quale esprimo la mia gratitudine più profonda: Lei è stata per me fonte di ispirazione e colei che, nonostante sia stata mia insegnante solo per un anno, mi ha convinto ad intraprendere questo faticoso ma meraviglioso percorso di studi.
Un ringraziamento speciale va alla mia famiglia, che mi è sempre stata accanto e non mi ha mai fatto mancare il suo sostegno in ogni mia decisione durante tutti questi anni. Ringrazio soprattutto mamma e papà, modelli di vita e di amore, che mi hanno cresciuto spronandomi a seguire sempre i miei sogni e aiutandomi a realizzarli. Senza di voi non sarei diventata quella che sono oggi, vi ringrazio perché per me siete i migliori genitori del mondo.
Ringrazio ovviamente anche la mia sorellina Stella, fedele compagna di giochi e premurosa confidente, la quale mi ha sempre sostenuto e confortato nei momenti più difficili. Nelle fredde giornate invernali padovane, mi hai aiutato a non scoraggiarmi nonostante la lontananza.
Un caloroso ringraziamento a Zia Sanna, la mia "fata madrina", che mi ha sempre rallegrato le giornate con la sua gioia e fantasia anche nelle fredde e umide serate padovane. Sei la zia che ogni bambino desidera, grazie di tutto.
Ringrazio i nonni, per avermi preparato le tantissime scorte di cibo necessario alla mia sopravvivenza a Padova in questi tre anni. Ma soprattutto vi ringrazio per i vostri insegnamenti e per il vostro affetto che non mi avete mai fatto mancare, è anche grazie a voi se oggi sono riuscita a realizzare uno dei miei sogni.
Ringrazio tutti gli altri parenti (che sono tanti!) che hanno sempre avuto fiducia in me e che sono stati presenti nei momenti importanti della mia vita.
Ringrazio le mie amiche padovane, in particolare Marica, Elisa e Anna, che hanno condiviso con me i momenti più divertenti e i più tristi, standomi sempre vicino e facendomi sentire davvero a casa. Quando sono partita per Padova non sapevo che cosa avrei trovato ma grazie a voi questi tre anni sono stati tra i migliori della mia vita. Ringrazio inoltre tutte le altre ragazze del Collegio Universitario del Sacro Cuore e le suore che, a modo loro, hanno avuto un ruolo importante nella mia vita universitaria.
Ringrazio i miei amici di facoltà, che mi hanno supportato (e sopportato) nei miei momenti di ansia pre-esame.
Infine ringrazio tutte le altre persone non menzionate che hanno avuto un peso determinante nel conseguimento di questo risultato, punto di arrivo di un percorso importante ma contemporaneamente punto di partenza di un nuovo ed entusiasmante percorso della mia vita.
Grazie a tutti.